Compton scattering of photons from bound electrons: Full relativistic independent-particle-approximation calculations

P. M. Bergstrom, Jr.*
Department of Physics and Astronomy, University of Pittsburgh, Pittsburgh, Pennsylvania 15260

T. Surić†
Department of Physics and Astronomy, University of Pittsburgh, Pittsburgh, Pennsylvania 15260 and Ruđer Bošković Institute, 41000 Zagreb, Croatia

K. Pisk‡
Ruđer Bošković Institute, 41000 Zagreb, Croatia

R. H. Pratt§
Department of Physics and Astronomy, University of Pittsburgh, Pittsburgh, Pennsylvania 15260
(Received 25 January 1993)

Compton scattering from bound electrons is studied within external field quantum electrodynamics and the independent-particle approximation (IPA), but without making use of any additional approximations, such as the impulse or incoherent-scattering factor approximations. Our calculations of the doubly differential cross section for scattering of unpolarized and polarized photons from bound atomic electrons as a function of scattered photon energy and angle are based on a numerical evaluation of the second-order S matrix in self-consistent screened atomic potentials. Such calculations permit the simultaneous discussion of all regions of the Compton spectrum for scattering from any atomic subshell. We present a systematic theoretical investigation of this process for atomic inner subshells at energies where binding effects in these subshells are important. We also discuss the efficient evaluation of the total atom scattering cross section in these cases. For individual subshells, we discuss the applicability of widely used approximate methods with regard to the spectral features they describe. For the K shell, we compare with earlier attempts at calculations within the relativistic S-matrix framework. We also discuss the cross section singly differential in scattered photon angle, emphasizing the contribution of terms neglected when making the incoherent-scattering factor approximation, as well as implications for total cross sections and for attenuation coefficients. Finally we discuss several recent experiments, including the efforts to find the infrared rise for soft photons.

PACS number(s): 32.80.Cy

I. INTRODUCTION AND GENERAL CONSIDERATIONS

In this paper we discuss the inelastic scattering of photons from bound atomic electrons, which results in ionization of an atom. We numerically evaluate the relativistic second-order S matrix for this process within the framework of external field quantum electrodynamics and the independent-particle approximation (IPA). A preliminary report on this procedure and some representative numerical results have already been presented [1–4]. We concentrate here on scattering from inner-shell electrons at incident photon energies where more approximate methods are not useful. Results are given for both polarized and unpolarized photons.

The recent availability of intense tunable photon sources and new methods of data analysis have stimulated considerable recent interest [5–10] in measuring such inelastic-scattering cross sections on bound atomic electrons. The Compton process serves as a probe of the atomic environment, as in condensed matter; it must also be understood to interpret the information about astrophysical and fusion plasmas contained in spectra of radiation emitted by or scattered from these plasmas. The process presents an instructive and, in principle, soluble example of the response of a composite system to perturbation.

Compton scattering is, however, one of the few low-order photon–bound-electron interaction processes that has thus far resisted a reasonably accurate and systematic treatment. While there have been attempts to evaluate the relativistic second-order S matrix for this process [11,12], these calculations were performed for only a few physical situations and were not tested against known limiting cases. The reason for the lack of a more comprehensive treatment is the presence of difficulties, encountered separately in calculating other atomic processes such as bremsstrahlung and Rayleigh scattering, which are encountered simultaneously in calculations of inelastic scattering. As in the calculation of bremsstrahlung, accurate numerical calculations of the Compton scattering spectrum require calculating many thousands of slowly converging integrals over three oscillating functions. The efficient evaluation of such integrals commands much current interest [13]. An additional

difficulty present in calculations of Compton scattering, which also occurs in elastic photon–bound-electron scattering calculations, is the evaluation of the relativistic Green's function in a spherically symmetric atomic potential. New methods to evaluate these Green's functions are still being considered [14]. In this paper we employ the inhomogeneous wave-function approach, which had previously been successfully used in elastic scattering [15]. It is apparent then that much effort and computer time must be invested in order to successfully and systematically calculate Compton scattering amplitudes. The availability of high-speed supercomputers (in our case the CRAY Y-MP and the Connection Machine CM-5) has facilitated the task. In this paper, we begin a more systematic attempt to understand Compton scattering. A detailed description of the theoretical basis for our results is given. Some discussion of the validity of more approximate approaches is presented along with an examination of previous attempts to evaluate the relativistic second-order S matrix for this process. Finally, we use our code as a tool to understand the results of recent Compton scattering experiments [5–9].

It is helpful to begin by remembering that inelastic scattering of photons is one of the primary processes responsible for the attenuation of radiation in matter. Other processes responsible for photon attenuation include elastic scattering, photoionization, and the production of pairs. Generally, the photoionization cross section dominates attenuation at low incident photon energies and pair production at higher energies, leaving a broad range of intermediate energies where inelastic scattering is the dominant absorptive mechanism. The range of energies where one or another of these processes is dominant depends also on the details of the scatterer, in our case roughly on the charge. Estimates of the importance of these processes for various elements suggest that inelastic scattering is more important than other absorptive mechanisms for energies of a few MeV in the heaviest elements. This range broadens considerably in lighter elements, being from a few keV to 100 MeV for a hydrogen atom. In these intermediate energy ranges, scattering occurs from all electrons with the innermost electron contributions dominating the soft-photon portion of the spectrum and the outer electrons dominating the peak region and the total scattering cross section [3]. Previous treatments of attenuation have assumed Compton scattering is adequately described in impulse approximation, as the scattering from a momentum distribution of free electrons; in situations that Compton scattering is the dominant attenuation mechanism it often can be well described simply as scattering from free electrons. By contrast the interest in scattering from bound electrons, as in this paper, primarily concerns the situation that the scattered photon is observed and conveys information about the structure of the target.

We choose the independent-particle approximation (IPA), in which all electrons move in a common self-consistent central potential, to describe our electron states. While the IPA neglects many electron effects such as electron-electron correlations, these are not usually important at electron energies considered here. The IPA has been successfully applied to other atomic processes at these energies, such as photoeffect, bremsstrahlung, and elastic scattering, and it has been customarily used in other, more approximate, treatments of inelastic scattering. There are certain regimes, which will be outlined below, where the IPA will not give an adequate quantitative description of inelastic scattering. Even in these cases some qualitative understanding is often obtained by application of the IPA.

Our calculations, as described in the next section, are fully relativistic. But many of the issues and features of the process can be discussed at a nonrelativistic level. Nonrelativistically, the Hamiltonian for the interaction of the radiation field with an electrically charged particle is given by [16]

$$H_{\rm int}=\frac{e^2A^2}{2}-e\mathbf{p}\cdot\mathbf{A}\ . \tag{1}$$

For scattering this leads to the Kramers-Heisenberg-Waller (KHW) matrix element [17]

$$M_{\rm KHW}=(\boldsymbol{\varepsilon}_1\cdot\boldsymbol{\varepsilon}_2^*)\langle f|e^{i(\mathbf{k}_1-\mathbf{k}_2)\cdot\mathbf{r}}|i\rangle-\sum_n\frac{\langle f|e^{-i\mathbf{k}_2\cdot\mathbf{r}}(\boldsymbol{\varepsilon}_2^*\cdot\mathbf{p})|n\rangle\langle n|e^{i\mathbf{k}_1\cdot\mathbf{r}}(\boldsymbol{\varepsilon}_1\cdot\mathbf{p})|i\rangle}{E_n-(E_i+\omega_1+i\varepsilon)}$$
$$-\sum_n\frac{\langle f|e^{i\mathbf{k}_1\cdot\mathbf{r}}(\boldsymbol{\varepsilon}_1\cdot\mathbf{p})|n\rangle\langle n|e^{-i\mathbf{k}_2\cdot\mathbf{r}}(\boldsymbol{\varepsilon}_2^*\cdot\mathbf{p})|i\rangle}{E_n-(E_i-\omega_2)}\ . \tag{2}$$

Here $|f\rangle$ and $|i\rangle$ are IPA solutions to the Schrödinger equation for the final and initial states of the electronic wave functions, respectively. The sum over intermediate IPA states $|n\rangle$ is a sum over a complete set of intermediate states, including orbitals which are occupied in the initial atomic configuration. Within this nonrelativistic context the sum includes only states corresponding to positive-energy states of the relativistic theory. The sum over the negative-energy states in the relativistic theory reduces to the first term of Eq. (2), which corresponds to a first-order evaluation of the A^2 term of the interaction Hamiltonian (1). The remaining two terms correspond to the $\mathbf{p}\cdot\mathbf{A}$ term of (1) evaluated in second-order perturbation theory. In the KHW matrix element (2), $|E_i|$ is the binding energy of the electron before scattering, $\boldsymbol{\varepsilon}_1$ and $\boldsymbol{\varepsilon}_2$ are the polarization vectors of the incident and scattered photons, and ω_1 and ω_2 are the energies of the incident and scattered photons.

If the final electronic state is the initial state ($|f\rangle=|i\rangle$, $\omega_1=\omega_2$), one has the KHW matrix element for Rayleigh

(elastic) scattering. The leading term is simply the form factor; the remaining two terms have been analytically evaluated for the case of the Coulombic K, L, and M states in the dipole approximation [18] and including all multipoles and retardation contributions for the ground state [19]. (The elastic process, $\omega_1=\omega_2$ but $|f\rangle\neq|i\rangle$, scattering without energy transfer but with change of magnetic substate, has also been derived from the corresponding relativistic amplitude using approximate Coulombic Green's functions [20].)

Inelastic scattering occurs when the electron changes state and energy (i.e., $|f\rangle\neq|i\rangle$, $\omega_1\neq\omega_2$). For a one-step scattering process, within the IPA, the inelastic scattering cross section may be further broken down into scattering with ionization of the atom and scattering with excitation of the atom. Compton scattering is the topic of this paper and this term has the conventional meaning that the final state of the system includes an electron ejected from the atom, a vacancy in the atom and the scattered photon. The vacancy may be filled, resulting in the emission of an additional photon or electron by fluorescence or Auger decay. Scattering where the final electron is bound is called Raman scattering. This process is resonant when ω_1 is equal to the energy required to make an upward transition from the initial state to the final bound state. While this terminology seems quite natural from the IPA viewpoint, much confusion persists. The reason is that for certain scattered photon energies and scattering states (when ω_2 corresponds to the downward transition energy from an occupied state of the initial electron configuration to a lower occupied or unoccupied state), the Compton scattering cross section is resonant and mimics the resonant behavior of Raman scattering. Here the Compton process is called alternatively resonant Raman scattering or resonant Raman-Compton scattering [21].

Each term of the KHW matrix element [Eq. (2)] accounts for a different feature in the Compton spectrum. These features are shown schematically in Fig. 1(a) (this figure represents a realistic case of Compton scattering from the $L2$ subshell, as will be shown below). Using a plane-wave final state, it is easily seen that a separate evaluation of the first term (the seagull term) yields a totally differential cross section dependent (aside from kinematic factors) only on the momentum density of the scattering charge. For a nodeless initial state, this results in a single peak centered at the average momentum of the state. For wave functions with additional nodes, subsidiary peaks may in principle be observable [22]. As will be outlined below, a number of different theoretical approaches including the impulse and A^2 (so-called form factor) approximations have been used to evaluate this term [22–31]. The two remaining terms in the KHW matrix element (the pole terms) have been evaluated, in a Coulomb field, by Gavrila and co-workers for the K shell [32], the L shell [33], and for any nS electron [34]. The second term of the KHW matrix element was shown to be divergent for soft scattered photons in the zero energy limit. This "infrared divergence" is expected on quite general grounds [35,36] and in the soft-photon region the Compton matrix element is directly proportional to the photoeffect matrix element. The third term contributes resonant behavior to the spectrum. The term resonant Raman or resonant Raman Compton (RRC) scattering is often used to describe these resonances which occur at scattered photon energies corresponding to fluorescence lines of downward transitions from the initial electronic configuration. The initial and final states of the system are the same as in Compton scattering. We therefore treat RRC as part of the Compton spectrum within the limitations of the IPA [37] in this paper, and we use the term resonant Raman Compton scattering.

The most general quantity which may be measured or observed in Compton scattering is the cross-section differential in the energy and angle of one of the particles (say the scattered photon) and in the angle of the other particle (the corresponding ejected electron), for specified photon polarizations, ejected electron spin, bound-electron subshell, and magnetic substate. Due to the difficulties of measuring this process, involving a coin-

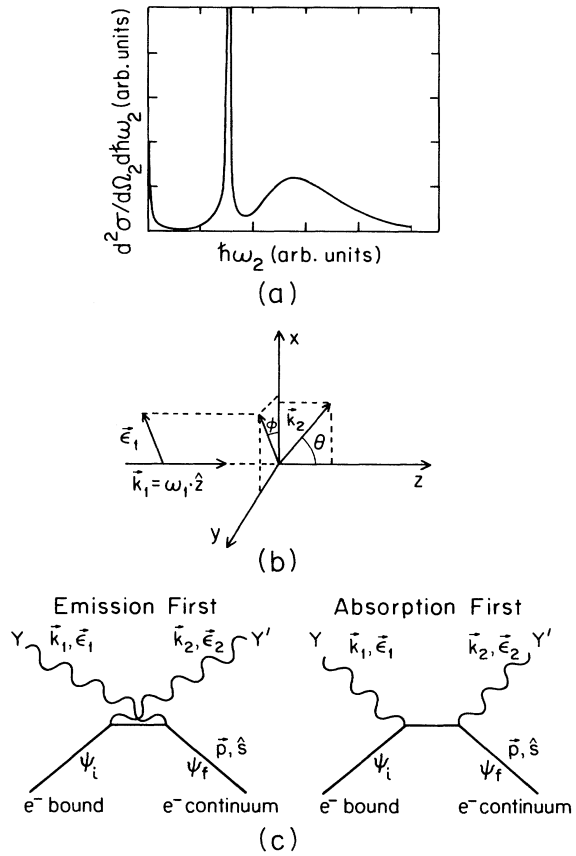

FIG. 1. (a) Schematic presentation of various spectral features in a Compton scattering process; divergence behavior for soft outgoing photons, resonant behavior near characteristic x-ray energies, and broad Compton peak for hard outgoing photons. (b) Scattering geometry considered here. The scattering plane is defined by the incoming and outgoing photon direction. θ is the scattering angle and ϕ is the angle between the vector of incoming photon linear polarization and the scattering plane. (c) Furry diagrams for the second-order amplitudes of the Compton scattering process.

cidence of the ejected electron and the scattered photon, the most commonly measured quantities are the energy and momentum (angle) of the scattered photon [38]. However, the scattered photon is sometimes detected in coincidence with a fluorescence photon emitted when an inner-shell vacancy is filled, permitting determination of the scattering subshell. (Anisotropies in the fluorescence distribution can provide information on the magnetic substate from which scattering occurred [39].) The quantities measured when the coincidence mode is used are the cross sections doubly differential in photon energy and angle or the cross-section differential in photon angle for a particular subshell. If the fluorescence photon is not observed, the measured cross section contains contributions from all energetically allowed subshells of the atom. Experiments have generally used traditional nuclear sources of unpolarized photons at relatively high energies (typically 59.54, 279.1, and 661.6 keV). Recently, the use of radiation from synchrotron sources (prepared in a high degree of linear polarization) in scattering experiments has made it possible to perform studies of this process in regimes inaccessible to these nuclear sources [4–6] and as a function of incident photon energy. While the results presented here are for Compton scattering where the ejected electron is not observed (but both for coincidence with the fluorescence photon, permitting determination of the scattering subshell, and for total atom scattering), we wish to point out the recent coincidence measurements of the scattered photon and the ejected electron of Rollason *et al.* [10]. We are aware of only one other reported measurement of the ejected electron [40] at incident photon energies where binding effects are important. These $(\gamma,e\gamma)$ measurements indicate much promise in the use of scattering as a tool for investigating atomic structure. We are restricting our attention here at the IPA level to one-electron Compton ejection and are not considering multiple-electron Compton scattering. Such processes are related to one-electron Compton scattering in the same way that multiple electron photoeffect is related to ordinary photoeffect. In both cases the shake off mechanism may be invoked at high ejected electron energy.

Developments in Compton scattering theory and experiment have often proceeded hand in hand. The scattering of photons by free stationary particles, and of very-high-energy photons (several MeV) from bound electrons in the hard-scattered-photon regime, is normally adequately [41] described by the well-known relationship due to Compton [42]

$$\omega_c \equiv \omega_2 = \frac{\omega_1}{1+\omega_1(1-\cos\theta)} , \tag{3}$$

and the Klein-Nishina formula [43] for the singly differential cross section,

$$\left[\frac{d\sigma}{d\Omega_2}\right]_{\mathrm{KN}} = \frac{\alpha^2}{2}\left[\frac{\omega_2}{\omega_1}\right]^2\left\{\frac{\omega_1}{\omega_2}+\frac{\omega_2}{\omega_1}-\sin^2\theta\right\} , \tag{4}$$

where θ is the scattering angle as defined in Fig. 1(b).

However, early experimental data for scattering of lower-energy photons from bound electrons revealed that the scattered photon energy is not uniquely determined by the incident photon energy and scattering angle. The spectrum of photons scattered from electrons bound to atoms was found to be dominated by a peak structure broadened and shifted slightly from the free Compton scattered photon energy ω_c. Early theoretical calculations were directed towards explaining this broadening and shift (defect). The work of DuMond [44] is a remarkable example of the combination of theory and experiment to make use of scattering as a tool to answer fundamental questions about the properties of matter. DuMond used semiclassical arguments about the effects of the momentum density of the scatterer on the scattering process in order to distinguish between several different descriptions of the core and valence electrons in beryllium. In this work one finds the beginnings of the most widely used approximation to the Compton scattering process, the impulse approximation (IA).

The description of the doubly differential cross section (in photon energy and angle) in this (often dominant) peak region of the spectrum has witnessed the greatest theoretical effort. Schnaidt [24] evaluated this cross section for the K shell using only the first or A^2 term of the KHW matrix element [Eq. (2)]. His A^2 or form-factor approximation made use of the exact Coulombic nonrelativistic wave functions for the initial and final states. Bloch [25] soon extended this approach, deriving exact formulas for scattering from arbitrary initial states. He evaluated these formulas approximately for the K and L shells in order to determine the Compton defect, i.e., the variation of the peak energy from the energy predicted by Eq. (3). Randles [26] used Coulombic relativistic wave functions in this A^2 term of the nonrelativistic matrix element and obtained a semirelativistic form-factor approximation for the ground state of a hydrogenic ion. Similar results were obtained independently by Pradoux *et al.* [31]. Schumacher and co-workers extended this approach to any s subshell [28]. Further work using exact nonrelativistic Coulomb eigenfunctions may be found for the L shell [22] and finally for any subshell [29]. These point-Coulombic approximations have proven to be useful in the peak region at low energy. However, for cases corresponding to the scattering of high-energy photons of traditional nuclear sources from the K-shell electrons of high-Z elements, differences occur between the predictions of the approaches using relativistic wave functions and those using nonrelativistic wave functions. It has not been possible to distinguish between these predictions experimentally.

While such use of Coulombic wave functions in evaluating the A^2 matrix element is instructive, the most widely used approximation for the doubly differential Compton scattering cross section has been the impulse approximation [22,27,30,45]. A purely nonrelativistic impulse approximation may be derived from the A^2 term of the KHW matrix element, treating the final electron state as a plane wave and considering the initial electron to be free with the momentum distribution of the bound state. Within this approximation we have [45]

$$\frac{d^2\sigma}{d\omega_2 d\Omega_2} = \alpha^2\left[\frac{1+\cos^2\theta}{2}\right]\frac{\omega_2}{\omega_1}\frac{1}{k}J_{nl}(p_z) , \tag{5}$$

where

$$J_{nl}(p_z)=\tfrac{1}{2}\int_{p_z}^{\infty} dp\, p\rho_{nl}(p)\ . \tag{6}$$

In these expressions $\rho_{nl}(p)$ is the bound-electron momentum density, k is the momentum transferred to the atom in the scattering process, $J_{nl}(p_z)$ is called the Compton profile of the state with quantum numbers n and l, p_z is the component of the initial (bound) electron momentum on the photon momentum transfer required by energy and momentum conservation for free particles, given in terms of the physical observables of the scattering process as

$$p_z=\frac{\omega_1-\omega_2}{k}-\tfrac{1}{2}k\ . \tag{7}$$

The impulse approximation has been argued to be valid for $ka_0\gg 1$ [27].

Another commonly used version of the impulse approximation is the relativistic impulse approximation (RIA), given most generally by Ribberfors [30]. This approximation starts from a relativistic expression for the scattering of a photon beam colliding with a beam of electrons. The doubly differential cross section for the scattering of unpolarized photons from nonaligned bound electrons, observing only the scattered photon, is

$$\frac{d^2\sigma}{d\omega_2 d\Omega_2}=\frac{\alpha^2}{2}\frac{\omega_2}{\omega_1}\frac{1}{k}\int_{p_z}^{\infty}\frac{p\rho(p)X(p,\theta,\omega_1,\omega_2)}{E(p)}dp\ , \tag{8}$$

where X is a rather complicated expression given by Eq. (37) of Ref. [30], where $E=(p^2+1)^{1/2}$ and where

$$p_z=\frac{E(\omega_1-\omega_2)-\omega_1\omega_2(1-\cos\theta)}{k}\ . \tag{9}$$

This expression for the component of the bound-electron momentum in the direction of the photon momentum transfer has the same meaning as expression (7), except that it is derived using relativistic kinematics for free particles. The region of validity of the RIA has not been rigorously established. It has often been presumed to be valid in the same region as the IA ($ka_0\gg 1$). Recently, Surić [2] used heuristic arguments to give a more sensitive criterion for when the RIA adequately describes the peak region of the spectrum:

$$\frac{P_{\rm av}}{k}\le 1\ , \tag{10}$$

where k is the photon momentum transfer and

$$P_{\rm av}=(p_z^2+\tfrac{2}{3}\langle p^2\rangle)^{1/2}\ . \tag{11}$$

Here p_z is given by Eq. (7) or (9) and $\langle p^2\rangle$ is the expectation value of the square of the electron momentum for the initial (bound) electron state. $P_{\rm av}$ has the meaning of the average allowed momentum which contributes to scattering photons into angle θ with energy ω_2 [p_z is fixed by Eq. (7) or (9)]. The criterion (10) differs from the usual criterion as it reflects the sensitivity of the peak region to $|p_z|$. It should be added that (as our results presented below will show) when Eq. (10) is satisfied the IA well describes the peak region under the additional condition that the low-energy theorem value [Eq. (13) below] there is very small. Less general relativistic impulse approximation calculations have been given by Eisenberger and Reed [46] and by Manninen, Paakkari, and Kajante [47].

The use of the IA (both nonrelativistic and relativistic) has been widespread partly due to the fact that calculations may be performed for any subshell, once wave functions for that subshell have been obtained. While this formalism has also been applied to scattering from the whole charge distribution of the atom, care must be taken to avoid problems which may occur when subshells contribute past their kinematic limit. This problem occurs because the shape of the spectrum in the peak region is assumed to be a function of the momentum transfer. At low momentum transfer, however, the peak region occurs at the extreme hard-photon edge of the spectrum and the inner subshells should not contribute due to kinematic considerations. Unfortunately, tables [45] of whole-atom profiles given as functions of p_z will not work in this regime as they ignore this problem of kinematic limits. To avoid this problem one cannot use the total charge density above, but sum subshell charge densities each with its own kinematic limit.

Other approximations using the A^2 term of the KHW matrix element are directed towards describing departures from the relativistic Klein-Nishina formula [Eq. (4)]. The singly differential cross section, observing only the direction but not the energy of the scattered photon, is commonly written in terms of the incoherent-scattering factor $S(x)$ (where x is the momentum transfer) [23,48] as

$$\frac{d\sigma(\omega_1,\theta)}{d\Omega_2}=S(x)\left[\frac{d\sigma}{d\Omega_2}\right]_{\rm KN}\ . \tag{12}$$

This singly differential cross section is in fact undefined, due to the infrared divergence for soft scattered photons mentioned above. However, the usual incoherent-scattering factor approximation is obtained from the A^2 term of the KHW matrix element (in which no infrared divergence is present) and may be calculated by integrating over an A^2 approximation for the doubly differential cross section [49]. Whittingham [11], in his relativistic S-matrix calculations, assumed an arbitrary low-energy cutoff in order to define $S(x)$. We are primarily concerned here with calculation of the doubly differential cross section and we will only briefly discuss the singly differential cross section, assuming a low-energy cutoff, and also discussing its relation to the radiative corrections to atomic photoeffect.

While measurement stimulated theoretical development of predictions for the peak region of the Compton spectrum, the opposite held true in the infrared and resonant regions of the spectrum. Gavrila's initial nonrelativistic Coulombic K-shell $\mathbf{p}\cdot\mathbf{A}$ calculations [32] showed that an infrared divergence, which could have been anticipated on general grounds [35,36], occurs in lowest nonvanishing order perturbation theory in the soft final photon limit. This spectral feature occurs for radiative processes which become indistinguishable from a corresponding radiationless process in the region of sufficiently

soft photons. In such a region one may relate the matrix element of the radiative process to the corresponding radiationless process, factoring out the divergent behavior in the soft-photon region. This low-energy theorem has been used in relating the cross section of electron bremsstrahlung in the soft-photon region to elastic scattering of electrons [35,50,51]. Recently, it has been used in the soft-photon region of Compton scattering [1,3,52], where the doubly differential cross section may be written

$$\frac{d^2\sigma}{d\omega_2 d\Omega_2}=\frac{\alpha v_f^2}{(2\pi)^2}\frac{1}{\omega_2}\int d\Omega_f \frac{[1-(\hat{\mathbf{p}}_f\cdot\hat{\mathbf{k}}_2)^2]}{[1-v_f(\hat{\mathbf{p}}_f\cdot\hat{\mathbf{k}}_2)]^2}\frac{d\sigma^{\rm pe}}{d\Omega_f} . \tag{13}$$

In Eq. (13) $d\sigma^{\rm pe}/d\Omega_f$ is the photoeffect differential cross section and v_f is the velocity of the ejected electron. While at energies below experimental resolution the divergent region of the Compton spectrum must be included with other divergent radiative corrections to the photoeffect, yielding a finite radiative correction to photoeffect [53], Gavrila's calculation prompted experimental searches which seemed to confirm the soft-photon rise feature of the Compton spectrum [54,55]. Recent measurements, however, have produced seemingly contradictory results [5–7].

The subsequent Coulombic L-shell calculations of Costescu and co-workers [33] also show the expected infrared divergence in this soft-photon region. Indeed the infrared divergence is characteristic of the soft-scattered-photon spectrum for any subshell. A new feature in the L shell was the resonant behavior which can be expected from the third term in the KHW matrix element (2). Separate resonances exist in all higher shell cross sections. The resonant Raman Compton feature has been investigated experimentally [6,56] and some L- and M-shell resonances have been observed.

In Sec. II we present the method we have used to calculate Compton scattering cross sections, relegating some formal points to an appendix. We apply this method to all regions of the spectrum in inner atomic subshells, discussing the use of more approximate methods. We find that the soft-photon region is often adequately described by results obtained from the photoeffect angular distribution in the low-energy theorem. The relativistic impulse approximation appears to be the most successful more approximate method in describing the peak region of the spectrum. We also discuss the validity of adding the cross sections from these separate methods. For the K shell we discuss other attempts at relativistic S-matrix calculations [11,12]. We integrate our results over scattered photon energies in order to obtain cross sections singly differential in scattered photon angle. We choose different low-energy cutoffs to this integration in order to discuss the contribution of infrared divergent terms to this quantity. We apply the understanding gained in our theoretical investigation of the inner-shell cross sections in order to discuss the contributions of these electrons and outer-shell electrons to whole atom cross sections. We also present an example of using an S-matrix approach to calculate scattering from all atomic electrons.

In Sec. III, we use our code to discuss representative recent experiments [5–9]. These experiments sample the broad range of interests in inelastic scattering from inner-shell electrons. Among them are traditional scattering experiments utilizing relatively high photon energies from nuclear sources on high-Z elements [8,9] and an experiment with photons from a lower-energy nuclear source scattering from the K-shell electrons of an intermediate-Z element. In these cases, the contribution of the peak region is of primary concern. We also examine experiments using lower-energy synchrotron sources on elements of intermediate Z in the K shell [5], where the infrared divergence and peak region contributions are both examined, and in higher shells [6], where the infrared divergence and resonant behavior are the primary spectral features. We confine our discussion to experiments where the observed spectrum is dominated by inner-shell contributions. Therefore, we do not discuss whole-atom measurements in the peak region of the spectrum. We present our conclusions in Sec. IV.

II. THEORY

We present a systematic procedure for performing calculations of cross sections for the Compton scattering of photons from electrons bound in atoms, starting from the second-order relativistic S-matrix element in the IPA. Our method is general in that it may be used for calculating scattering from any subshell in the atom and, unlike earlier approximate treatments, over the whole spectrum of scattered photon energies. While these calculations may be performed for incident photons of arbitrary polarization, we concentrate on cases where the incident photon beam is unpolarized or linearly polarized, corresponding to situations which have been investigated experimentally. We limit our discussion to cases where the ejected electron and the polarization of the scattered photon are not observed. The measured final-state observables are the scattered photon energy, the scattered photon angle, and the subshell (but not the magnetic substate) from which scattering occurred. In Fig. 1(b) we present the scattering geometry considered here. Our calculations represent the results of scattering from a given subshell and so correspond to experiments in which the scattered photon has been detected in coincidence with a fluorescence photon emitted when the vacancy created in the scattering subshell is filled by a radiative transition. In order to obtain results for the whole atom [3], corresponding to the experimental situation where the fluorescence photon is not detected, these results must be summed over all subshells.

We evaluate the independent-particle approximation to the external field QED matrix elements corresponding to the Furry diagrams in Fig. 1(c). The second-order amplitude for this process may be written

$$M_{\rm fi}=M_a+M_e . \tag{14}$$

In this expression M_a is the contribution to the amplitude of the second Furry diagram in Fig. 1(c). This absorption first matrix element may be written

$$M_a=-4\pi\alpha i\int d^3x\,d^3y\,\bar{\psi}_f(\mathbf{y})\boldsymbol{\gamma}\cdot\mathbf{A}_2^*(\mathbf{y})\times S_F^{\text{ext}}(\mathbf{y},\mathbf{x},E_i+\omega_1)\boldsymbol{\gamma}\cdot\mathbf{A}_1(\mathbf{x})\psi_i(\mathbf{x})\ . \quad (15)$$

In this expression the subscripts 1, 2, i, and f refer to variables associated with the incident and scattered photons and the initial bound and final continuum electrons, respectively. Within the Furry picture the wave functions of the electron and the propagator include the effects of the IPA potential to all orders. This is accomplished by solving for these objects in the field of the nucleus and the other atomic electrons. Here we obtain these quantities in realistic spherically symmetric atomic potentials $V(r)$. In some cases that we discuss a Coulombic potential is used. However, in most cases a self-consistent screened Dirac-Fock-Slater (DFS) atomic potential with a Latter tail has been employed. These potentials were obtained using the code of Liberman, Cromer, and Waber [57]. The corresponding amplitude for the emission-first diagram of Fig. 1(c) may be written

$$M_e=-4\pi\alpha i\int d^3x\,d^3y\,\bar{\psi}_f(\mathbf{y})\boldsymbol{\gamma}\cdot\mathbf{A}_1(\mathbf{y})\times S_F^{\text{ext}}(\mathbf{y},\mathbf{x},E_i-\omega_f)\boldsymbol{\gamma}\cdot\mathbf{A}_2^*(\mathbf{x})\psi_i(\mathbf{x})\ . \quad (16)$$

As has been discussed above, the calculation of the propagator in the field is one of the complicating features of this problem. We do not evaluate the propagator directly, rather we follow the method of Brown, Peierls, and Woodward [15] and define the function

$$F(\mathbf{y},\eta)=-\int d^3x S_f^{\text{ext}}(\mathbf{y},\mathbf{x},\eta)\boldsymbol{\gamma}\cdot\mathbf{A}(\mathbf{x})\psi_i(\mathbf{x})\ , \quad (17)$$

which is the solution of the inhomogeneous differential equation

$$[\boldsymbol{\alpha}\cdot\mathbf{p}+\beta+V(|\mathbf{y}|)-\eta]F(\mathbf{y},\eta)=\boldsymbol{\alpha}\cdot\mathbf{A}(\mathbf{y})\psi_i(\mathbf{y})\ . \quad (18)$$

Here η is the energy of the propagator of the relevant Furry diagram. We may then express the amplitudes (10) and (11) in terms of the solution of this differential equation as

$$M_a=4\pi\alpha i\int d^3y\,\bar{\psi}_f(\mathbf{y})\boldsymbol{\gamma}\cdot\mathbf{A}_2^*(\mathbf{y})F(\mathbf{y},E_i+\omega_1)\ , \quad (19)$$

$$M_e=4\pi\alpha i\int d^3y\,\bar{\psi}_f(\mathbf{y})\boldsymbol{\gamma}\cdot\mathbf{A}_1(\mathbf{y})F(\mathbf{y},E_i-\omega_2)\ . \quad (20)$$

We assume spherical symmetry of the atomic potential in order to decompose into partial waves the wave function of the ejected electron and of the function $F(\mathbf{y},\eta)$, as discussed in the Appendix, yielding the results Eqs. (A4), (A9), and (A12). We also decompose the photon wave functions into multipoles [see Eq. (A7)] and are thus able to express our matrix elements as the sum of terms given by products of angular integrals, which may be straightforwardly evaluated in terms of Racah coefficients and phase factors, and of integrals of products of the radial components of the partial waves of the ejected electron, the solution of the inhomogeneous Dirac equation, and of the photon multipole. These radial integrals, given by Eq. (A16), are not rapidly convergent for the absorption first matrix element, as the solution of the inhomogeneous Dirac equation has continuumlike character. One of the methods chosen here to evaluate the integrals has been used before in calculations of Compton scattering [11] and bremsstrahlung [58]. In some limiting cases, for very soft photons, the asymptotic integration was performed numerically using a complex coordinate method.

The fully differential cross section for the Compton scattering process is

$$d^3\sigma=|S_{\text{fi}}|^2 d\omega_2 d\Omega_2 d\Omega_f\ . \quad (21)$$

Here

$$S_{\text{fi}}=2\pi M_{\text{fi}}\delta(E_f+\omega_2-E_i-\omega_1)\ . \quad (22)$$

Our code calculates the differential cross section which describes an experimental situation in which polarized photons are scattered from unaligned electrons bound in a particular subshell. As discussed, the ejected electron is not observed nor is the polarization of the scattered photon. The absolute square of the matrix element Eq. (14) is summed analytically over final photon polarizations and final electron-spin and angular momentum states, averaged over initial bound-electron magnetic substates. We are able to write the doubly differential cross section for the inelastic scattering of linearly polarized photons from bound electrons into given scattering angle and fixed energy in the form

$$\frac{d^2\sigma}{d\omega_2 d\Omega_2}=\alpha^2 N\sum_{J=0}^{\infty}C_J^0 P_J^0(\cos\theta)+C_J^2 P_J^2(\cos\theta)\cos(2\phi)\ , \quad (23)$$

where N denotes the number of electrons occupying a particular subshell and $P_J^{0,2}$ are the associated Legendre polynomials.

Our code evaluates the coefficients C_J^0 and C_J^2, which, for $\omega_2<2-E_B$, are given by the expressions

$$C_J^0=\frac{2J+1}{2(2j+1)}\sum_{[e,e',\gamma,\gamma']}S_J^{[\gamma]}\begin{bmatrix}L_1' & L_1 & J\\ 1 & -1 & 0\end{bmatrix}\{(-1)^{\lambda_1}\sigma_1^{[e,e',\gamma,\gamma']}I_e^{[e,\gamma]}I_e^{[e',\gamma']}$$
$$+(-1)^{L_1+L_2+\lambda_1'+\lambda_2}\sigma_2^{[e,e',\gamma,\gamma']}(\mathrm{Re}I_a^{[e,\gamma]}\mathrm{Re}I_a^{[e',\gamma']}+\mathrm{Im}I_a^{[e,\gamma]}\mathrm{Im}I_a^{[e',\gamma']})$$
$$+(-1)^{\lambda_1}\sigma_3^{[e,e',\gamma,\gamma']}I_e^{[e,\gamma]}\mathrm{Re}I_a^{[e',\gamma']}\}, \quad (24a)$$

$$C_0^2=C_1^2\equiv 0\ ,$$

$$C_J^2=\frac{2J+1}{2(2j+1)\sqrt{(J+2)(J+1)J(J-1)}}\sum_{[e,e',\gamma,\gamma']} S_J^{[\gamma]}\begin{bmatrix} L_1' & L_1 & J \\ 1 & 1 & -2\end{bmatrix} \times\{\sigma_1^{[e,e',\gamma,\gamma']} I_e^{[e,\gamma]} I_e^{[e',\gamma']}+(-1)^{L_1'+L_2'+\lambda_2'}\sigma_2^{[e,e',\gamma,\gamma']} \times(\mathrm{Re}I_a^{[e,\gamma]}\mathrm{Re}I_a^{[e',\gamma']}+\mathrm{Im}I_a^{[e,\gamma]}\mathrm{Im}I_a^{[e',\gamma']}) +\sigma_3^{[e,e',\gamma,\gamma']} I_e^{[e,\gamma]}\mathrm{Re}I_a^{[e',\gamma']}\}\ , \tag{24b}$$

where

$$S_J^{[\gamma]}=(-1)^{(L_1+L_2+L_1'+L_2'+\lambda_1+\lambda_2+\lambda_1'+\lambda_2')/2+1}[(2L_1+1)(2L_2+1)(2L_1'+1)(2L_2'+1)]^{1/2} \times\tfrac{1}{2}[1+(-1)^{(L_2+L_2'+\lambda_2+\lambda_2'+1)}]\tfrac{1}{2}[1+(-1)^{(L_1+L_1'+\lambda_1+\lambda_1'+J)}]\begin{bmatrix} L_2' & L_2 & J \\ 1 & -1 & 0\end{bmatrix},$$

$$\sigma_1^{[e,e',\gamma,\gamma']}=(-1)^{(L_1+L_2+\lambda_2'+j+j_2+J)}\begin{Bmatrix} j_1 & j_1' & J \\ L_2' & L_2 & j\end{Bmatrix}\begin{Bmatrix} j_1 & j_1' & J \\ L_1' & L_1 & j_2\end{Bmatrix},$$

$$\sigma_2^{[e,e',\gamma,\gamma']}=(-1)^{(j+j_2+J)}\begin{Bmatrix} j_1 & j_1' & J \\ L_1' & L_1 & j\end{Bmatrix}\begin{Bmatrix} j_1 & j_1' & J \\ L_2' & L_2 & j_2\end{Bmatrix},$$

$$\sigma_3^{[e,e',\gamma,\gamma']}=2(-1)^{(j_1+j_1'+\lambda_2')}\begin{Bmatrix} L_1' & L_1 & J \\ j & j_1 & L_2 \\ j_1' & j_2 & L_2'\end{Bmatrix}.$$

In these expressions the symbol $[e]$ denotes the set of electron angular momentum quantum numbers ($[e]=[\kappa_1,\kappa_2]$), where subscript 1 refers to the electron propagator and subscript 2 refers to the outgoing electron. Similarly, the symbol $[\gamma]$ denotes the angular momentum quantum numbers of both photons ($[\gamma]=[L_1,\lambda_1,L_2,\lambda_2]$). Subscripts 1 and 2 refer to incoming and scattered photons. The primed values have the same significance; they occur in the absolute square of the matrix element. $I_e^{[e,\gamma]}$ denotes radial integrals corresponding to the emission-first matrix element and $I_a^{[e,\gamma]}$ denotes radial integrals corresponding to the absorption-first matrix element. For the energies considered here, the $I_e^{[e,\gamma]}$ are real (they become complex for $\omega_2>2-E_B$). The $I_a^{[e,\gamma]}$ are generally complex numbers and $\mathrm{Re}I_a^{[e,\gamma]}$ and $\mathrm{Im}I_a^{[e,\gamma]}$ denote their real and imaginary parts. The explicit expressions of these integrals in terms of solutions of inhomogeneous radial Dirac equations, outgoing electron radial components, and photon radial components are given in the Appendix.

Our code numerically solves inhomogeneous Dirac equations for partial-wave components of the F function, solves homogeneous Dirac equations for partial-wave components of the Ψ_e function, and calculates radial integrals $I_e^{[e,\gamma]}$ and $I_a^{[e,\gamma]}$ (A16a) and (A16b). We use these radial integrals for calculating the coefficients $C_J^{0,2}$ of Eq. (23) for the doubly differential cross section for an incident polarized photon beam. To obtain the unpolarized differential cross section we have to average over incident photon polarizations. Effectively this means dropping the terms in C_J^2, and we obtain the doubly differential cross section for unpolarized radiation

$$\frac{d^2\sigma}{d\omega_2 d\Omega_2}=\alpha^2 N\sum_{J=0}^{\infty} C_J^0 P_J^0(\cos\theta)\ . \tag{25}$$

In the remainder of this section we use the S-matrix computer code, based on this Compton scattering formalism, to investigate the cross section doubly differential in scattered photon energy and angle, considered as a function of energy for fixed angle. Our purpose is to develop an understanding of inner-shell cross sections in regimes where they may not be calculated adequately by any single more approximate treatment. We then use the understanding gained from this effort in order to establish accurate methods for calculating cross sections for Compton scattering of photons from all of the electrons bound in atoms or ions.

We also integrate our Compton spectra over scattered photon energies in order to determine the cross section singly differential in scattered photon angle. We may discuss the contributions to this singly differential cross section from spectral features which are not normally included. These features are the soft-scattered-photon divergence and the resonances in the doubly differential cross section. They result from evaluation of the $\mathbf{p}\cdot\mathbf{A}$ term in the nonrelativistic interaction Hamiltonian, while the singly differential cross section has typically been obtained by integrating the contribution of the peak region of the spectrum, which is derived from the A^2 contribution to the nonrelativistic amplitude. In the next section we integrate the singly differential cross section over scattering angles in order to obtain the total cross section for this process.

Our investigation of Compton scattering starts with

the K shell. The K-shell doubly differential cross section exhibits only two of the three spectral features discussed above. These features are the soft-photon rise of the spectrum and the Compton peak; the resonant effect is possible only in the L and higher shells. The questions which we seek to answer are when one or another of these spectral features is dominant and when some combination of these features is necessary to describe the spectrum. There are a number of different approximate methods available to calculate K-shell cross sections. We investigate which of these approximations best describes the doubly differential cross section. Finally, some previous attempts at S-matrix calculations for the K-shell doubly differential cross section are discussed [11,12]. We also discuss the singly differential cross section for K-shell Compton scattering. The principal effects which we examine are the contribution of soft scattered photons and the adequacy of various A^2 approximations in describing this quantity.

We then consider scattering from L-shell electrons. The L-shell doubly differential cross section may contain all three features discussed above (although the resonant effect is relatively weak in the L1 subshell). We examine the validity of approximate methods for L-shell calculations. We also discuss the effect of screening in the L shell. We discuss results for the L-shell singly differential cross sections, including the effect of the K-L resonances on this quantity.

Finally, we present methods for combining the cross sections from the various subshells in order to obtain cross sections for Compton scattering from all of the electrons in a given atom or ion. One may simply sum the S-matrix results over all of the atomic electrons. This method is inefficient in general, however, because of the large computational effort necessary in outer shells, which are often adequately described in their dominant regions by approximate methods. We discuss which combination of approximate methods may be used in place of full S-matrix calculations for outer-shell electrons.

The computer code developed to implement the formalism described above is necessarily complex, making it essential to have tests of all steps of the procedure in all spectral regions. No single test is so comprehensive. Rather it was necessary to compare against approximate methods in regions where those approximations are known to hold and to develop additional tests for aspects left unaddressed by such comparisons. The approximate methods chosen for our initial tests were those methods which may be derived from the KHW matrix element without significant further approximations. The nonrelativistic point-Coulombic dipole results of Gavrila and co-workers for the K [32] and L [33] shells are expected to be good, over the entire scattered photon spectrum, for $Z\alpha \ll 1$ and $Z\alpha\omega_i/E_B \ll 2$. These results are also valid, for higher incident photon energies, in the soft-scattered-photon part of the spectrum. A corresponding dipole calculation using our code checks the operation of the homogeneous and inhomogeneous differential equation solvers and radial integral solvers in our code. For the hydrogen atom agreement between Gavrila's K-shell calculations and our code, using a point-Coulombic potential and the dipole term only, was within 0.1% over the spectrum. For the L shell similar agreement was found in the cases which were run. In order to gain confidence in the multipole expansions of the photons' wave functions, the partial-wave expansions of the propagator and the continuum electrons and the angular momentum coupling, additional multipoles need to be taken. The A^2 approximation, which includes all photon multipoles, describes the peak region of the spectrum for high incident photon energies. In Fig. 2 we show results in this region for the scattering of very high-energy photons (2.5 keV or nearly 200 times the binding energy) from the K shell of hydrogen. Excellent agreement is evident both in the near forward and backward directions. In order to more rigorously test these aspects of the code at energies of experimental interest, where approximations based on the KHW matrix element do not apply, we performed a separate analytic calculation of the Compton cross section in the Born approximation. (The same approximation has been used by Owen [27], but with some additional simplifications which were not completely justified by the author.) This corresponded to setting the potential equal to zero in the calculation of the solution of the inhomogeneous wave equation and in calculating the final electron state. We made these assumptions in our code for a wide range of photon energies (15 eV to 600 keV) and for a wide range of Z. These independent Born approximation calculations always agreed within 0.1%. At the highest energies in this range a very large number of multipoles contribute to the cross section, lending confidence to the part of our code which combines the matrix elements and the angular momentum coefficients to get the coefficients of the expansion of the cross section.

As we have discussed, there are numerous theories available for calculating K-shell Compton scattering spectra. We have chosen to analyze only the most commonly used [24,30,32,45]. Where no adequate theory is available, we present new approximate methods for calculating the Compton spectrum. In the peak region of

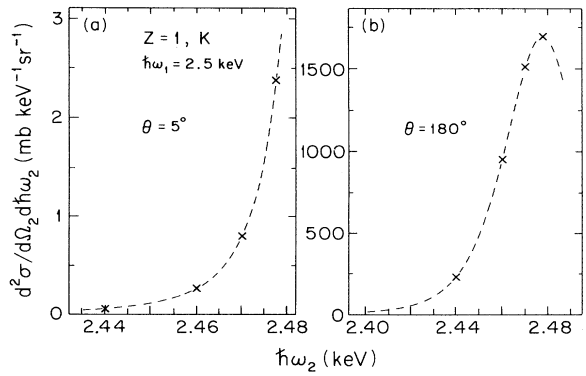

FIG. 2. Doubly differential cross section for the scattering of 2.5-keV photons from the ground state of hydrogen into (a) 5° and (b) 180°. Shown here are the S-matrix calculations ($\times$) and the nonrelativistic form factor (dashes), i.e., $\mathbf{A}^2$ approximation.

the Compton spectrum, the most familiar approaches are the nonrelativistic A^2 or form-factor approximation (FF) [24], the impulse approximation (IA) [45], and the relativistic impulse approximation (RIA) [30]. In addition to the fact that these methods are employed fairly often to calculate the Compton scattering doubly differential cross section, they represent different levels of approximation to the problem. The form-factor approximation is an exact evaluation, using solutions of the Schrödinger equation for an electron in a Coulomb or screened field, of the A^2 term in the nonrelativistic amplitude. The impulse approximation is derived from this term under the further assumption that the final electron may be described by a plane wave, enabling one to write the cross section in terms of the momentum distribution of the scattering state. This approximation is generally evaluated numerically, using screened wave functions. In what follows, when we present impulse approximation results, we use the tabulated values of Biggs, Mendelsohn, and Mann [45]. These tables are the most extensive available and have been calculated using bound-electron wave functions similar to those chosen in our S-matrix calculations. They are widely used. Finally, we consider the relativistic impulse approximation due to Ribberfors [30]. This approximation is derived from a relativistic treatment of the scattering of photons from free moving electrons [36]. As with the IA, the resulting expression for the RIA is written in terms of the momentum distribution of the scattering electron. In the RIA calculations given here we use momentum distributions obtained from the same wave functions which have been used in our S-matrix calculations. The difference between the IA and the RIA lies in the fact that the RIA uses relativistic kinematics.

At the time of our initial calculations, the only available theoretical results in the soft-scattered-photon region were those of Gavrila [32]. This theory is an exact evaluation of the $\mathbf{p}\cdot\mathbf{A}$ terms of the nonrelativistic amplitude, using Coulombic wave functions and the Coulomb Green's function. Numerical results were obtained in the dipole approximation only. In addition to our S-matrix calculations, in this work we present cross sections obtained from photoeffect angular distributions using the low-energy theorem Eq. (13) (LET). These calculations include the effects of screening and all contributing photon multipoles and have been used to successfully describe the full S-matrix calculations for low scattered photon energies [1,3].

The question of which feature dominates the K-shell Compton spectrum of a particular element for given incident photon energy and scattering angle is possible to answer using simple arguments. The kinematic limit of the spectrum (i.e., the maximum scattered photon energy), equals the incident photon energy minus the binding energy of the scattering shell. In order for the maximum of the peak to be part of the observed spectrum, it must shift to kinematically allowed scattered photon energies. The shift of this peak for bound electrons is equal to the free electron Compton shift to lower energies, given by Compton's formula Eq. (3), added to the Compton defect (taken here to be Bloch's value $E_B/6$ shifted to higher energies [25], as cited in Ref. [59]). For energies of several hundred keV and larger the Compton peak will be visible for most angles. We may derive an approximate expression for when the center of the Compton peak will appear which gives

$$\omega_1 > \left[\frac{7E_B}{6(1-\cos\theta)}\right]^{1/2} . \tag{26}$$

As has been stated above, the free Compton line is broadened by the momentum of the bound electron. The half-width of the resulting peak is of the order of the electron binding energy. This means that the onset of the peak may be observed, for fixed scattering angle, at somewhat lower energies, in the form of a cross section rising until the cutoff is reached. Examination of Eq. (26) reveals that the center of the peak cannot be observed for forward scattering and is more likely to be observable (at fixed incident photon energy) for large scattering angles. The contributions due to the $\mathbf{p}\cdot\mathbf{A}$ terms monotonically decrease with increasing scattered photon energy. Additionally, as these contributions may be expressed in terms of the photoeffect matrix element, which decreases rapidly in magnitude with increasing incident photon energy, they show a corresponding decrease with increasing incident photon energy. Usually, one expects the Compton peak to be the dominant feature when it is shifted to observable energies, with the crossover to infrared rising behavior at lower scattered photon energies. In order for there to be comparable contributions from both terms, the peak must shift to low scattered photon energies for incident photon energies not far from the ionization threshold. This situation is possible only for scattering at several times threshold from high-Z elements.

In Fig. 3, we present results for the doubly differential cross section for the scattering of 2.94 keV photons from an electron bound in the K shell of carbon (the results given in this paper will be per electron unless otherwise noted) into 0°, 60°, 120°, and 180°. The incident photon energy is approximately 10 times the energy needed to ionize a K-shell electron. However this energy is still smaller than that needed to shift the maximum of the Compton peak into the kinematically observable range (9 keV for 180°) as predicted by Eq. (26). So the free Compton peak (represented by the vertical arrow) remains outside the kinematically allowed range of scattered photon energies for K-shell electrons. The maximum shift of the peak to lower energies (0.04 keV at 180°) is smaller than the expected shift of the peak to higher energies due to the Compton defect (approximately 0.05 keV). Therefore one does not expect the cross section at the end point to be within the halfwidth of the bound Compton peak. Indeed, the extreme hard-photon region of the spectrum only gives the onset of the peak [if one carries the impulse approximation calculation for this case past the kinematic limit of the shell (as in incoherent-scattering function calculations) to the incident photon energy, the integrated peak intensity is approximately 50 times the peak intensity shown]. In this region, the nonrelativistic form-factor approximation most adequately reproduces the spectrum. The IA and the RIA are indistinguishable for this case. While these approximations qualitatively

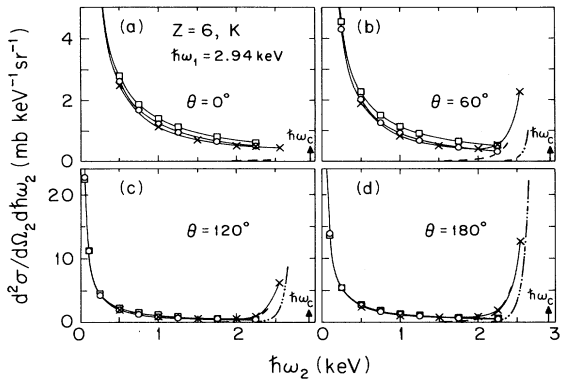

FIG. 3. Doubly differential cross sections for the scattering of 2.94-keV photons from a K-shell electron of carbon into (a) 0°, (b) 60°, (c) 120°, (d) 180°. The cross sections shown are obtained from nonrelativistic form-factor calculations [24] (dashes), the nonrelativistic impulse approximation [45] (dotted line), the relativistic impulse approximation [30] (chain-dashed line), the results of the nonrelativistic $\mathbf{p}\cdot\mathbf{A}$ calculations of Gavrila [32] (circles), results obtained from photoeffect cross sections using the low-energy theorem [Eq. (13)] (boxes), and the results of the present S-matrix calculations ($\times$). The energy for Compton scattering by free electrons is shown by the vertical arrow. Lines through the symbols have been drawn to aid the eye. Note we are showing cross sections per electron, not for the filled subshell.

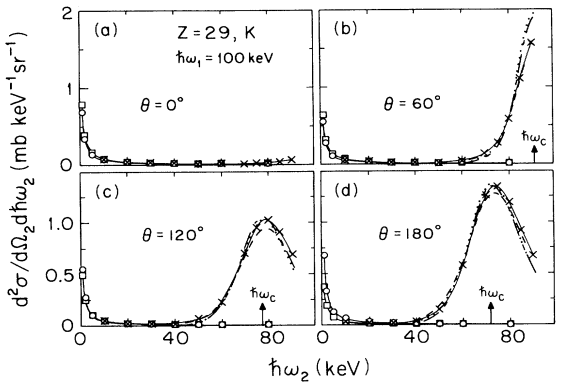

FIG. 4. Same as Fig. 3, except for the scattering of 100-keV photons from a K-shell electron of copper.

reproduce the cross section at the hard-photon end, the result appears shifted to higher scattered photon energies. We will see, subsequently, that this difference is not a shift but reflects the narrower Compton peak predicted within the impulse approximation.

For scattering from light elements, the shift of the Compton peak towards lower scattered photon energies with increasing angle is not large enough for the peak to be observable even though the incident photon energy is much larger than the threshold value. For higher incident photon energies, the Compton peak could shift to scattered photon energies which are kinematically allowed. At these higher incident photon energies, for finite angles, the Compton spectrum would be adequately described by the IA or RIA as the contributions from the $\mathbf{p}\cdot\mathbf{A}$ terms become much smaller, corresponding to the decrease in the photoeffect cross section.

We now consider, in Fig. 4, the scattering of 100-keV photons from the K shell of copper. This high incident photon energy results in a shift of the Compton peak greater than or equal to the binding energy for scattering angles larger than 60°. At back angles, the peak is almost completely visible and dominates the spectrum. The agreement of the RIA, the IA, and the form factor with the S-matrix calculations is excellent in this region, although the form factor is somewhat smaller at intermediate and large angles. While the low scattered photon energy portion of the spectrum and the entire spectrum for forward scattering are still given adequately by the low-energy theorem results, the cross sections in these regimes are much smaller than the peak region values.

In Fig. 5 the scattering of 279.1-keV photons from the K shell of lead is considered. This energy is approximately three times the binding energy of the scattering electron. In this case, several interesting departures from the results of the preceding cases are apparent. Although the peak is the dominant feature at most angles, contributions corresponding to the $\mathbf{p}\cdot\mathbf{A}$ terms are also significant, even in the peak region. Significant differences exist between the low-energy theorem results and those of Gavrila. The low-energy theorem results more adequately reproduce the S-matrix calculations in the soft-scattered-photon regime; these results are larger than the Gavrila results at forward angles and smaller at back angles. These differences between the low-energy theorem and Gavrila's result reflect the need for additional multipoles at these energies. Significant differences also exist between the relativistic impulse approximation and the impulse approximation. Neither theory shows systematic agreement with the S-matrix calculations.

It is appropriate at this juncture to discuss other calculations of Compton scattering from bound electrons performed within the framework discussed here, relativistic second-order QED. We are aware of two other calculations for the doubly differential cross section [11,12]. These calculations were performed only for K-shell scattering in a few cases. The methods of Whittingham are quite similar to those presented here. Wittwer used a

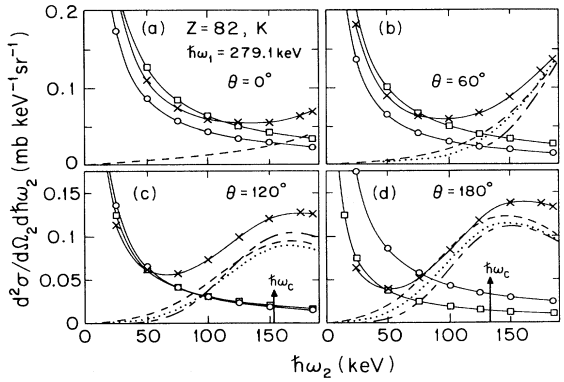

FIG. 5. Same as Fig. 3 except for the scattering of 279.1-keV photons from a K-shell electron of lead.

different, direct approach to calculating the propagator. As has been mentioned, we do not calculate the propagator directly, but instead solve the inhomogeneous wave equation. Neither of the previous attempts at an S-matrix calculation of Compton scattering mentions checks against known limiting cases.

The calculations of Whittingham [11] were performed for the scattering of 279.1- and 661.6-keV photons from the K shell of U, Pb, Ta, and Sm. These calculations used point-Coulombic potentials only and a limited number of multipoles were retained due to the limitations of the available computers. The propagator was not calculated directly but was included in the solution of the inhomogeneous wave equation, as in the present work, using Brown's method [15]. We have performed calculations with our code at 279.1 keV for Ta and for Pb and at 661.6 keV for Pb. (All calculations for these cases, with the exception of the IA, which uses the tables from Ref. [45], were performed in a point-Coulombic potential.) We have just seen, for the scattering of 279.1-keV photons from the K shell of lead (including screening), that none of the approximate theories which are commonly applied may give more than a qualitative description of the spectrum. We now consider the scattering of 279.1-keV photons from the K shell of Ta. This data is given in Fig. 6 for 60° and 120°. We also give the S-matrix results of Whittingham (solid line without data points). Again, no approximate method is adequate. Whittingham's results are larger than all other results for both 60° and 120°. This agrees with observations made in the point-Coulombic 279.1-keV lead case which has been presented elsewhere [1,2]. As in the screened lead case just discussed, Gavrila's results are smaller than those obtained using the low-energy theorem (which agree with our S-matrix calculations for small scattered photon energies) for forward scattering and bigger for backward scattering. This indicates that the discrepancy is due to the need for additional photon multipoles and not to screening corrections (the results are point-Coulombic). Significant differences between the IA and the RIA are evident. In Fig. 7 we present calculations for the scattering of 661.6-keV photons from the K shell of Pb into 60°

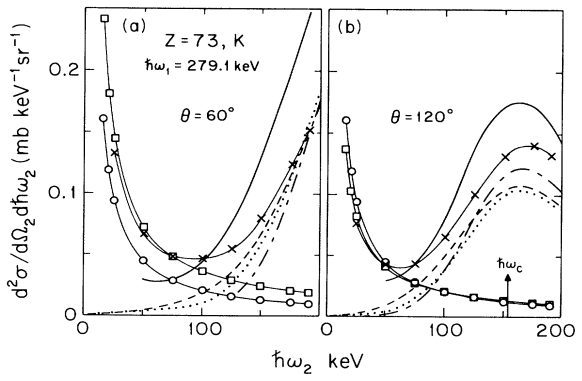

FIG. 6. Same as Fig. 3 except for the scattering of 279.1-keV photons from a K-shell electron of tantalum into (a) 60° and (b) 120°. Also shown are the S-matrix results of Whittingham [11] (solid line without data points).

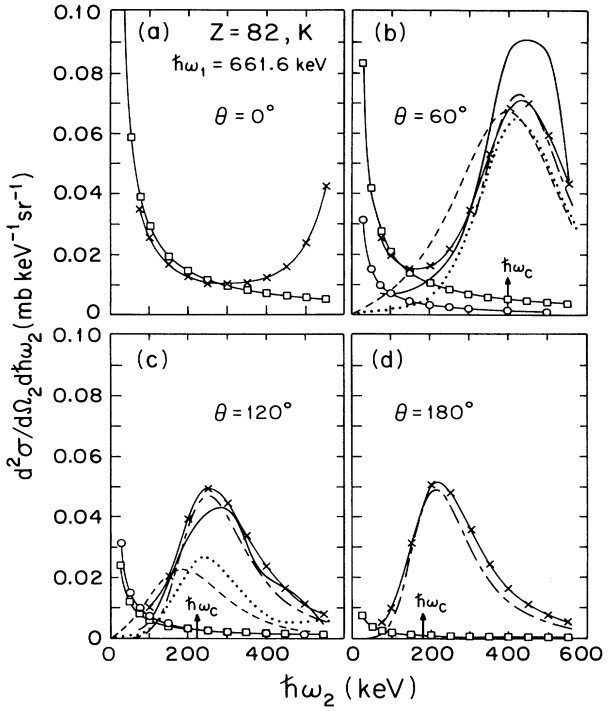

FIG. 7. Same as Fig. 3 except for the scattering of 661.6-keV photons from a K-shell electron of lead. Also shown are the S-matrix results of Whittingham [11] (solid line without data points).

and 120° (where Whittingham presented data) as well as for forward and backward scattering. We compare again with relativistic results obtained using the low-energy theorem and the RIA, with the nonrelativistic theories of Gavrila and Schnaidt and with the results given by Whittingham. The agreement in the peak region of the spectrum between the RIA and our results is excellent. At low scattered photon energies, agreement with the low-energy theorem results of Eq. (13) may be observed. Gavrila's calculations are not adequate here, as they are smaller than the LET calculations for forward angles and larger at back angles. The results of Whittingham and the nonrelativistic calculations (the form factor and the IA) differ substantially from our calculations and from each other, as in the case of scattering 279.1-keV photons from Ta and Pb. Here Whittingham's results are substantially larger than all others at 60° and are smaller than ours at 120°.

Wittwer [12] performed calculations for the scattering of 145-keV photons from the K shell of Sn and Au and for 320-keV photons from Au. These calculations used screened DFS atomic potentials. An interesting feature is the direct calculation of the propagator. This permitted the identification of spectral features in terms of corresponding contributions of the propagator. Wittwer found, as would be expected [60], that the peak region was described almost entirely by the sum over negative-energy intermediate states and that the infrared divergences was due to the sum over positive-energy intermediate states. This corresponds to the discussion

presented above describing the spectrum in terms of the KHW matrix element. Because we have not calculated the propagator directly here, we can make no similar identification. We can, however, test the separability of the S- matrix into the nonrelativistic components for certain cases. If one looks at the first term of the KHW matrix element [Eq. (2)], it is apparent that the peak contribution vanishes when ε_1 and ε_2 are perpendicular to each other. This orthogonality may be assured for a 90° scattering angle and a linearly polarized beam if the polarization vector of the incident beam lies in the plane defined by the incident and scattered beam momenta [corresponds to $\Theta=90°$, $\Phi=0°$ in Eq. (23)]. We demonstrate this effect for the scattering of 60-keV photons from the K shell of Ge in Fig. 8(a). The pluses indicate the S-matrix results when the polarization vector is in the plane of the beams and the circles indicate when it is out of the plane. The peak vanishes, as expected, for the case where the polarization vector is in the plane, confirming the approximate separability of the S matrix into its nonrelativistic analogs for this case. At higher incident photon energies, in scattering from high-Z elements, where the spectral features make comparable contributions, this separability may not exist. We demonstrate this in Fig. 8(b), for the scattering of 279-keV photons from the K shell of tin. Here, the peak in the polarized cross section appears even where it is not allowed in the nonrelativistic treatment (although it is not very large in magnitude).

In Fig. 9 we compare the same approximations that we have been examining and our calculations with those of Wittwer [12] for the scattering of 145-keV photons from Sn. The bars on the Wittwer data reflect his error estimates. The agreement between the S-matrix approaches is excellent, except for forward scattering, which is to be expected due to the limited number of multipoles used in Ref. [12]. In the forward direction, our results are in agreement with the LET. The center of the Compton

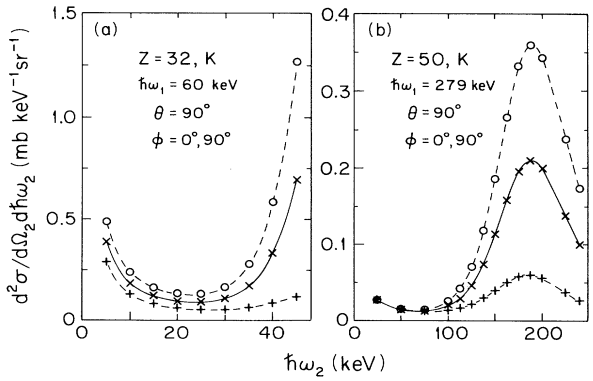

FIG. 8. Comparison of our S-matrix calculations for the scattering of polarized photons into 90° for the scattering geometry where the polarization vector of the polarized incident photon beam is (+) in the plane, (○) perpendicular to the plane defined by the incident and scattered photon momenta. Results for unpolarized photons (×) are also shown. (a) Scattering of 60-keV photons from a K-shell electron of germanium, (b) scattering of 279-keV photons from a K-shell electron of tin.

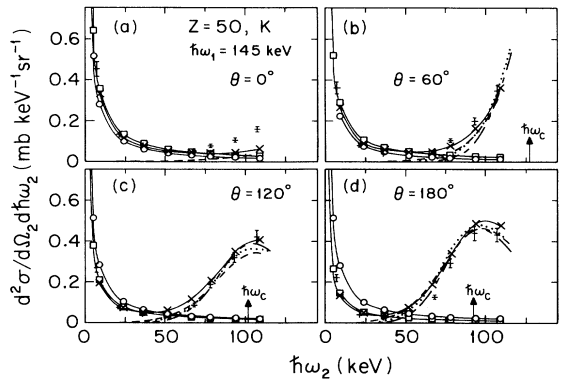

FIG. 9. Same as Fig. 3 except for the scattering of 145-keV photons from a K-shell electron of tin. The points with the error bars are the S-matrix calculations of Wittwer [12].

peak is observable at 120° and 180°. All peak region approximations give reasonable results in this regime. While the LET agrees with the S matrix at low photon energies and for forward scattering, the nonrelativistic dipole results of Gavrila [32] again are different. In Fig. 10 we present similar data for the scattering of 145-keV photons from Au. The level of agreement between S-matrix approaches here is even better than in the preceding case. The incident photon energy is not large enough here for the peak to make a significant contribution.

Finally, in Fig. 11, we consider the scattering of 320-keV photons from Au. Wittwer's S-matrix calculations are in agreement with ours, except for forward scattering. In the forward direction, our results may be obtained by adding the LET and the nonrelativistic form factor. In this case, the peak region is substantial at other angles. In the peak region the RIA, the IA, and the FF do not agree. The IA seems less adequate than the other approaches. At soft-scattered-photon energies the LET is in agreement with the S-matrix calculations. As in the other cases at relativistic energies, the nonrelativistic dipole calculations are smaller than the relativistic calculations in the forward direction and larger for scattering at back angles.

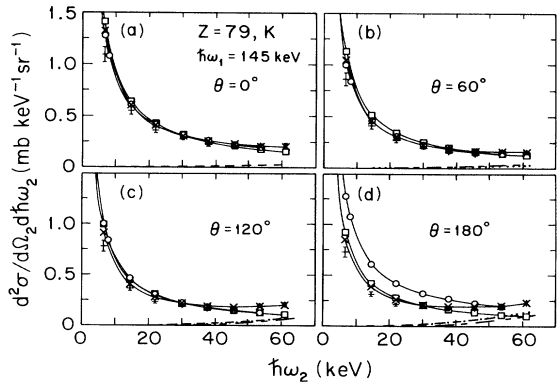

FIG. 10. Same as Fig. 3 except for the scattering of 145-keV photons from a K-shell electron of gold. The points with the error bars are the S-matrix calculations of Wittwer [12].

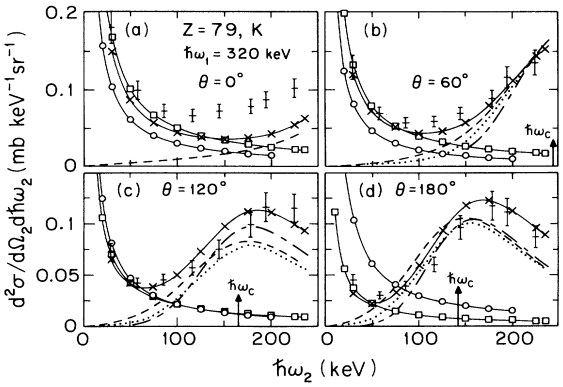

FIG. 11. Same as Fig. 3 except for the scattering of 320-keV photons from a K-shell electron of gold. The points with the error bars are the S-matrix calculations of Wittwer [12].

Usually, the Compton scattering doubly differential cross section may be obtained, to a good approximation, by adding the low-energy theorem results to the IA or RIA results for cross sections (although for light elements it may be preferable to use the nonrelativistic form-factor cross sections because of the narrower IA or RIA peaks). There are a number of reasons for this. For low-energy scattering, the spectral features are well separated and the intermediate region is relatively small in magnitude (any interference effects in that region are usually not observable). For high energies there may be regions where both terms contribute significantly. However, the contribution of the peak is real and the LET contributions have a phase given by $ie^{i\delta_l}$ [61], (where δ_l is the phase shift of the dominant partial-wave contribution to the ejected electron wave function). At the electron energies available, δ_l should be small, leading to a small interference term in the square of the sum of the amplitudes. We demonstrate this in Fig. 12. In the left panel, we plot the S-matrix results and the approximate methods which we have been examining. In the right panel we plot the S-matrix results and two curves representing the sums of approximate methods. The top curve is the sum of the nonrelativistic form-factor approximation and the dipole results of Gavrila. Clearly, this sum does not adequately reproduce the S-matrix results. This is not due to the need for an interference term, however. It may be seen that in this case, as for all high-energy, high-Z cases, the Gavrila results are inadequate, principally due to the dipole approximation made in those calculations. The sum of the low-energy theorem results and the relativistic impulse approximation results is in reasonable agreement with the S-matrix calculation, except where the RIA does not adequately reproduce the peak. This confirms that no interference term is necessary when adding the LET and the RIA in these high-energy, high-Z cases.

We may now summarize what we have learned about the K-shell Compton scattering doubly differential cross section. For light elements, at energies where departures from free Compton scattering may occur, cross sections generally decrease monotonically to the hard-photon end of the spectrum where only a small part of the peak may be observable. For elements of intermediate nuclear charge, larger parts of the peak become visible as the incident photon energies become large enough for the Compton peak to shift significantly and as the scattering angle increases. We did not observe significant discrepancies between relativistic and nonrelativistic approximations to the cross section in either the peak or soft-photon regions of the spectrum at low incident photon energies. For higher energies and heavier elements, discrepancies between the approximate methods and the S-matrix approach and between the various approximate methods exist. In the peak region, the RIA most adequately reproduces the S-matrix results; the IA is less adequate here. For soft-scattered-photon energies, the results of Gavrila consistently underestimate the cross section for forward angles and overestimate it at back angles. This is a result of the dipole approximation made in those calculations. The LET agrees very well with the S-matrix calculations for these energies. In general the peak region and the soft-scattered-photon behavior are well separated. We have explicitly demonstrated that these features are separable for most cases. However, for the scattering of photons with energies several times threshold from high-Z elements, both features may be present for all scattered photon energies. The simple addition of the approximate methods may give the S-matrix results (i.e., if the LET contribution is out of phase with the peak contribution). At higher energies, the contributions of the LET are small and the cross section is adequately given by the RIA.

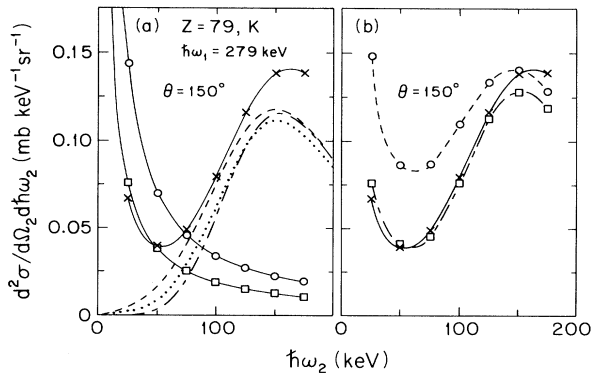

FIG. 12. Cross sections for the scattering of 279-keV photons from a K-shell electron of gold into 150°. (a) The cross sections shown are obtained from nonrelativistic form-factor calculations [24] (dashes), the nonrelativistic impulse approximation [45] (dotted line), the relativistic impulse approximation [30] (chain-dashed line), the results of the nonrelativistic $\mathbf{p}\cdot\mathbf{A}$ calculations of Gavrila [32] (circles), results obtained from photoeffect cross sections using the low-energy theorem (boxes), and the results of the present S-matrix calculations ($\times$). (b) For the same angle we present results obtained by adding the nonrelativistic form-factor calculations [24] and the nonrelativistic $\mathbf{p}\cdot\mathbf{A}$ calculations of Gavrila [32] (circles), results obtained by adding the relativistic impulse approximation [30], and the results obtained from photoeffect cross sections using the low-energy theorem (boxes), and the present S-matrix results ($\times$).

We turn our attention now to the cross section singly differential in scattered photon angle for this process. As has been discussed, for scattering from free electrons at rest, this cross section is given by the Klein-Nishina formula which predicts the intensity of the Compton line at each angle. A relativistic S-matrix calculation of this cross section was performed by Henry [62] for the scattering of several keV photons from the hydrogenic ground state. As we have seen in Fig. 2, the cross section in this case is well described by the nonrelativistic form factor [24]. Therefore we will not further discuss this result. The question that we will consider is how to define this cross section in the bound-electron case. It has usually been defined by integrating the A^2 term of the nonrelativistic doubly differential cross section over scattered photon energies. We have seen that these A^2 approximations may not adequately represent the spectrum even in the peak region. However, while the RIA is usually valid in the peak region of the spectrum, it does not adequately reproduce the S-matrix results over the entire spectrum. Simply integrating the S-matrix result over scattered photon energies is not possible due to the infrared divergence in the soft final photon limit. In order for the integrated S-matrix result to have physical meaning, a low-energy cutoff to the integration must be selected. This cutoff should be defined with regard to the physical situation being considered. One should consider experimental constraints such as the detector response and discriminator setting. Usually the experimental cutoff which is chosen is the K-shell photoionization threshold of lead. The reason for this is that at the high incident photon energies of the nuclear sources which are traditionally used, the bound-bound transitions in the lead shielding dominate the Compton signal. We shall show such cutoffs in the comparison with experiment. We shall also integrate our S-matrix results using two other cutoffs. The first cutoff that we choose, scattered photon energies equal to the binding energy of the scattering shell, is a practical experimental cutoff. Namely, below this energy many photons may be expected in the radiative decay of holes created by K-shell photoionization, which dominates the inelastic scattering cross section by orders of magnitude in most cases considered here. The Compton signal may be comparable to the uncertainty in the cross section of the dominant process, making it difficult to separate the effects. The other cutoff which we assume, 1% of the incident photon energy, has been chosen to give us an idea of the contribution of the low-energy region of the spectrum to the singly differential cross section.

In Fig. 13(a), we plot the singly differential cross section for the scattering of 2.94-keV photons from the K shell of carbon. Actually, we give the ratio (sometimes called the scattering factor) of the scattered photon singly differential cross section to the free-electron Klein-Nishina value. This ratio gives some idea of the relative efficiency of bound-electron scattering versus the free-electron process. The integrated RIA results are extremely small, as the Compton peak is not important in the spectra given in Fig. 3. While the S-matrix results, calculated using the cutoffs described above, are much larger than the RIA results, the angular distributions remain small relative to the scattering of photons from free electrons.

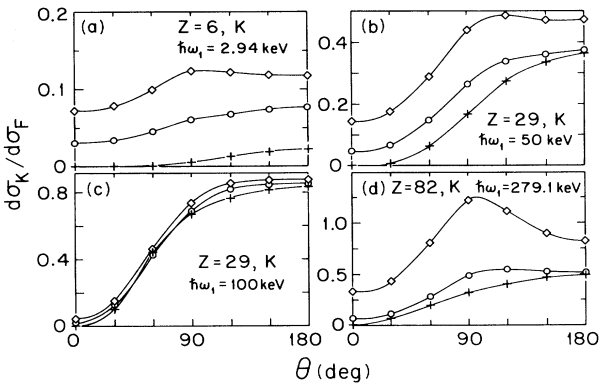

FIG. 13. (a) Ratios of the cross sections singly differential in scattered photon angle for the scattering of 2.94-keV photons from a K-shell electron of carbon to the free-electron cross sections. The singly differential cross sections were obtained from cross sections doubly differential in scattered photon energy and angle by integrating over the scattered photon energies. The theories used were the relativistic impulse approximation (+), and the present S-matrix calculations (circles and diamonds) (or low-energy theorem results and relativistic impulse approximation results were used where the S-matrix results were not available). The circles are calculated assuming a low-energy cutoff at the K-shell photopeak, the diamonds were obtained assuming a cutoff of 1% of the incident photon energy. (b) Same as (a) except for the scattering of 50-keV photons from a K-shell electron of copper. (c) Same as (a) except for the scattering of 100-keV photons from a K-shell electron of copper. (d) Same as (a) except for the scattering of 279.1-keV photons from a K-shell electron of lead.

In Figs. 13(b) and 13(c) we give the singly differential cross sections for the scattering of 50- and 100-keV photons from the K shell of copper. At 100 keV the three methods agree reasonably well, reflecting the small magnitude of the $\mathbf{p}\cdot\mathbf{A}$ contributions to the double differential cross section. At back angles, the scattering factor for 100-keV photons is nearly unity. This is expected as the full peak in the doubly differential cross section is nearly kinematically observable. For 50-keV photons the angular distributions reflect a mixed situation, where the peak region and the $\mathbf{p}\cdot\mathbf{A}$ terms make comparable contributions to the spectra.

Finally, in Fig. 13(d), we give the scattering factors for the scattering of 279.1-keV photons from the K shell of lead. In this case the contribution of the low-energy behavior below the K edge and of the spectrum above the K edge are comparable. At intermediate scattering angles, when one includes photons below the K edge, the scattering factor is greater than 1. This means that the bound electron is scattering photons more efficiently than free electrons would. The agreement of the integrated RIA result with the S-matrix result (which is cut off at the K edge) at back angles reflects the suppression of the $\mathbf{p}\cdot\mathbf{A}$ contributions for backscattering. These latter two results are smaller than unity, reflecting the facts that the

entire peak region is not kinematically allowed and that some of the peak region is below the low-energy cutoff.

Clearly, in most cases considered here, the singly differential cross sections for scattering from bound electrons is smaller than the free-electron Klein-Nishina result. At small scattering angles, the S-matrix results are nonzero. This is in accord with the behavior of the spectrum, which is nonzero for forward scattering. At larger angles, the major portion of the scattering factor is found by integrating the peak contribution. The ratio of the angular distribution to the free-electron result approaches one in cases where the peak is completely observable and where the low-energy behavior is negligible.

We now discuss the scattering of photons from L-shell electrons. L-shell spectra are more complicated than K-shell spectra because of the possibility of resonant behavior. As has been discussed, these resonances occur for scattered photon energies equal to the K-$L1$, K-$L2$, or K-$L3$ energy difference. These resonances are highly suppressed in the $L1$ subshell due to the dipole selection rules for bound-bound transitions. As with the K shell, kinematic arguments may be made for the position of the Compton peak in the spectrum. The L-shell Compton peak may be observed in some cases where the K-shell peak contribution is cut off because the lower L-shell binding energy means that the kinematic limit of the spectrum occurs at higher scattered photon energies. The variety of approximate methods available for the K shell also exists for the L shell. The range of applicability of some of these methods is more limited due to effects such as screening.

In Fig. 14 we consider the scattering of 2.94-keV photons from the $L1$ subshell of carbon. This energy is well above the K- and L-shell ionization thresholds. Also shown are the IA and RIA results, the $\mathbf{p}\cdot\mathbf{A}$ calculations of Gavrila and Tugulea [33], the low-energy theorem calculations in a point-Coulombic potential and in a screened potential. As in the K-shell case, much of the spectrum is dominated by the contributions of the $\mathbf{p}\cdot\mathbf{A}$ terms. However, the effects of screening in this regime are evident as the point-Coulombic results of Gavrila and Tugulea and the results obtained from the low-energy theorem using a point-Coulombic potential agree reasonably well, whereas the screened S-matrix calculation agrees with the low-energy theorem results obtained in the same screened self-consistent potential. Within a nonrelativistic formalism K-$L1$ resonant structure is strictly forbidden. In our relativistic S-matrix calculations such structure exists in principle, but is highly suppressed in this low-energy regime. We will show such resonances in a subsequent, more relativistic case. There we will see the K-$L1$ structure is negligible compared to K-$L2$ or K-$L3$ structure.

The IA and the RIA agree with each other and with the S-matrix results at the hard-photon end of the spectrum for finite angles. The values of the scattering cross section in the peak region are much larger here than in the K shell. This may be simply understood in terms of the impulse approximation. In terms of IA, the smaller average momentum means that the peak width is narrower than for the inner shell since the double differential

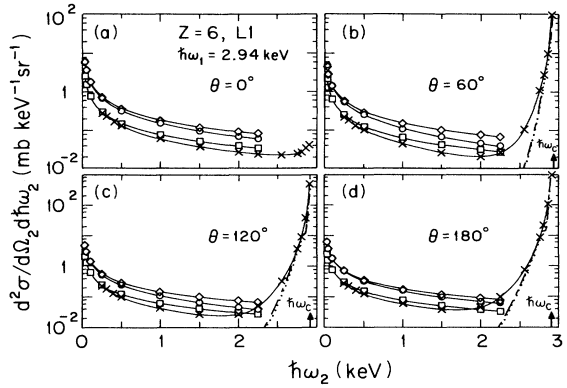

FIG. 14. Cross sections for the scattering of 2.94-keV photons from an $L1$ subshell electron of carbon into (a) 0°, (b) 60°, (c) 120°, (d) 180°. The cross sections shown are obtained from the nonrelativistic impulse approximation [45] (dotted line), the relativistic impulse approximation [30] (chain-dashed line), the results of the nonrelativistic $\mathbf{p}\cdot\mathbf{A}$ calculations of Gavrila and Tugulea [33] (circles), results obtained from photoeffect cross sections using the low-energy theorem in a screened potential (boxes) and in a point-Coulombic potential (diamonds), and the results of the present S-matrix calculations ($\times$). The energy for Compton scattering by free electrons is shown by the vertical arrow.

cross section, away from the peak, gets contributions from high momenta which are less probable for outer shells. The height of the peak is a measure of the average of the inverse magnitude of the momentum. Consequently, the peak height for an outer shell must be larger.

The situation is quite different for the $L2$ subshell. This may be observed in Fig. 15. The Compton peak region is still adequately given by both the IA and the RIA. However the rest of the spectrum is dominated by the K-$L2$ resonance at approximately 0.28 keV, which is much wider than the K-$L1$ resonance due to the dipole allowed transition. The low-energy theorem is adequate only for extremely soft-scattered-photon energies because, for higher energies, the S-matrix result is pulled to higher values by the resonance. Only below resonance do the S-

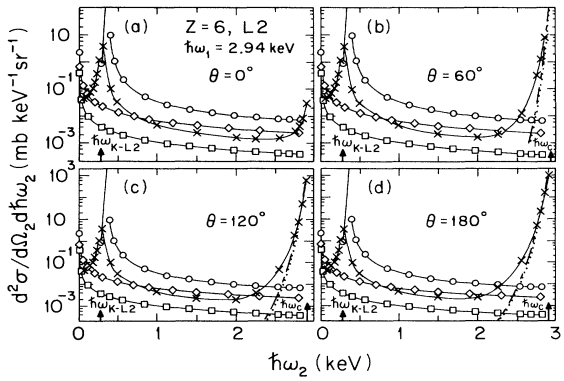

FIG. 15. Same as Fig. 14 except for $L2$ subshell. The energy for the characteristic K-$L2$ transition (in screened potential) is also shown by a vertical arrow.

matrix results approach the low-energy theorem calculations. The results of Gavrila and co-workers [33] also contain the resonant behavior. The position of the resonance is somewhat different corresponding to the difference between the screened relativistic energy levels used in the S-matrix calculations and the point-Coulombic nonrelativistic energy levels used in these results. The intensity of the resonance is angle-independent, as expected. Note the great difference in magnitude between Coulomb and screened results in this $L2$ case, which reflects the large ratio of small distance normalization values of Coulomb and screened bound-state wave functions.

In Figs. 16–19 we consider the scattering of 4, 8, and 15 keV photons from the $L1$ subshell of Ni. These energies are nearly one-half the K-shell binding energy, just below the K-shell binding energy, and almost twice the K-shell binding energy. The forward-scattering cross sections are given in Fig. 16. All of the spectra are simply given by the low-energy theorem behavior. For the 60° scattering angle of Fig. 17 one sees the onset of the Compton peak in the 8- and 15-keV spectra. In Figs. 18 and 19 (scattering angles of 120° and 180°, respectively), the peak is the dominant hard-photon end behavior for the two high-energy cases. In the peak region, the IA and the RIA are in close agreement with each other. We note here the flattening of the IA and RIA spectra. This flattening is the IA representation of the subsidiary maxima mentioned in the introduction. Due to the symmetry of the Compton profile about $p_z=0$ this flattening occurs on both sides of the peak within LA. However, in the more exact calculations of Bloch and Mendelsohn [22]

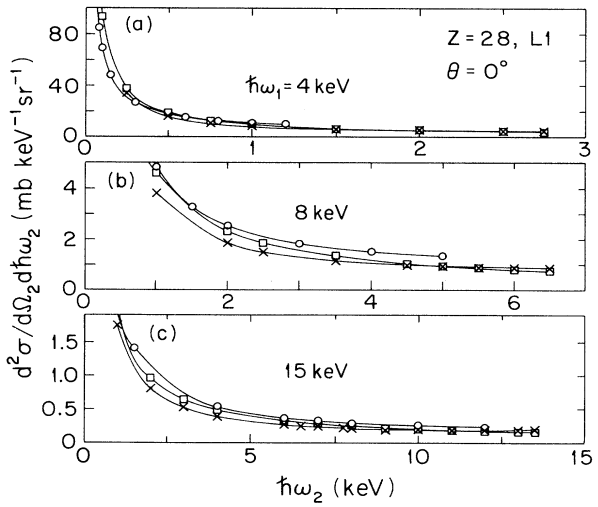

FIG. 16. Doubly differential cross sections for the scattering of (a) 4-keV photons, (b) 8-keV photons, and (c) 15-keV photons from an $L1$ subshell electron of nickel into 0°. The cross sections here are calculated within the nonrelativistic impulse approximation [45] (dotted line), the relativistic impulse approximation [30] (chain-dashed line), the results of the nonrelativistic $\mathbf{p}\cdot\mathbf{A}$ calculations of Gavrila and Tugulea [33] (circles), results obtained from photoeffect cross sections using the low-energy theorem in a screened potential (boxes), and the results of the present S-matrix calculations (×).

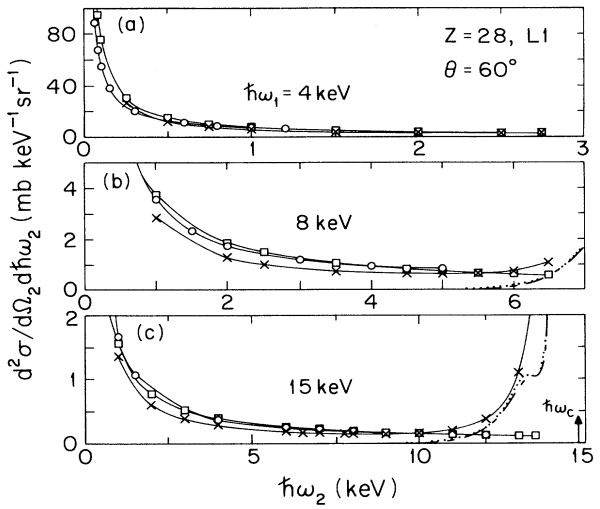

FIG. 17. Same as Fig. 16 except for a scattering angle of 60°. The energy for Compton scattering by free electrons is shown by the vertical arrow.

these subsidiary maxima were found only on the high-energy side of the peak. (In these examples such maxima above the peak are not kinematically accessible, but in other cases we have observed them.) The IA and RIA results agree with the S-matrix calculations only for the highest incident photon energy.

In Figs. 20–23, we give the $L2$ subshell contributions to the scattering spectra for these same photon energies and angles. Again, the $L2$ spectra are very different from the $L1$ results. For forward scattering, the spectra are not simply governed by the infrared behavior. In fact all three spectra have some of the resonant behavior. The shape of this resonance varies as the incident photon energy is tuned across the K edge. The intensity of the resonance at 15 keV is larger than at 8 and at 4 keV. At 4 keV, we are far off resonance and the resonant behavior is only observable as a slight upturn to the spectrum at the

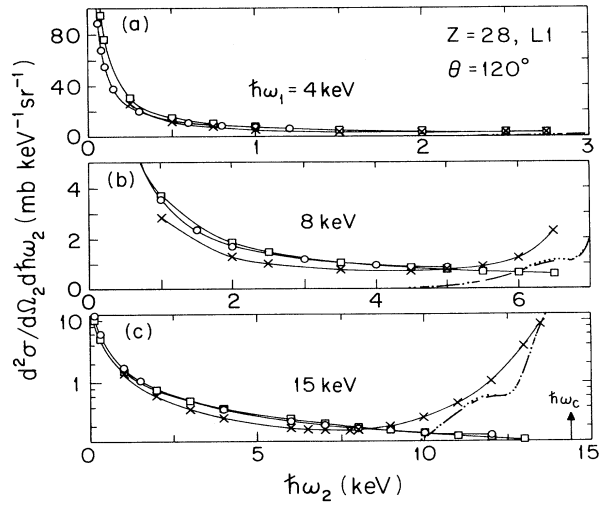

FIG. 18. Same as Fig. 17 except for a scattering angle of 120°.

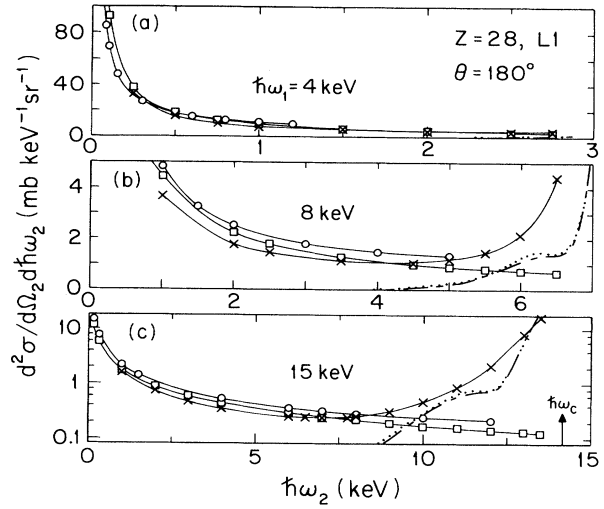

FIG. 19. Same as Fig. 17 except for a scattering angle of 180°.

hard-photon end and by the difference between this spectrum and the LET results. At 8 keV the resonance is quite intense and the spectrum deviates from the LET results by more than two orders of magnitude at the hard photon end. For larger angles, the 4- and 8-keV spectra do not change significantly. This is due to the fact that they are resonance dominated and to the fact that the resonances are not angle dependent. The resonance in the 15-keV spectra remains unchanged with increasing

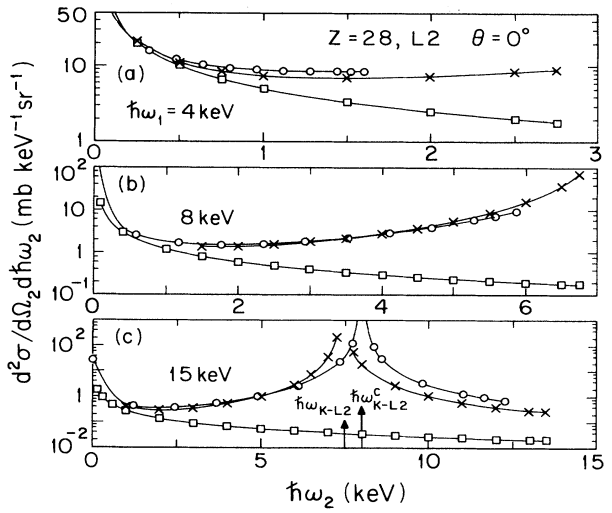

FIG. 20. Doubly differential cross sections for the scattering of (a) 4-keV photons, (b) 8-keV photons, and (c) 15-keV photons from an $L2$ subshell electron of nickel into 0°. The cross sections here are calculated within the nonrelativistic impulse approximation [45] (dotted line), the relativistic impulse approximation [30] (chain-dashed line), the results of the nonrelativistic $\mathbf{p}\cdot\mathbf{A}$ calculations of Gavrila and Tugulea [33] (circles), results obtained from photoeffect cross sections using the low-energy theorem in a screened potential (boxes), and the results of the present S-matrix calculations ($\times$). The energy for the characteristic K-$L2$ transition (both in screened and Coulomb potential) is shown by a vertical arrow.

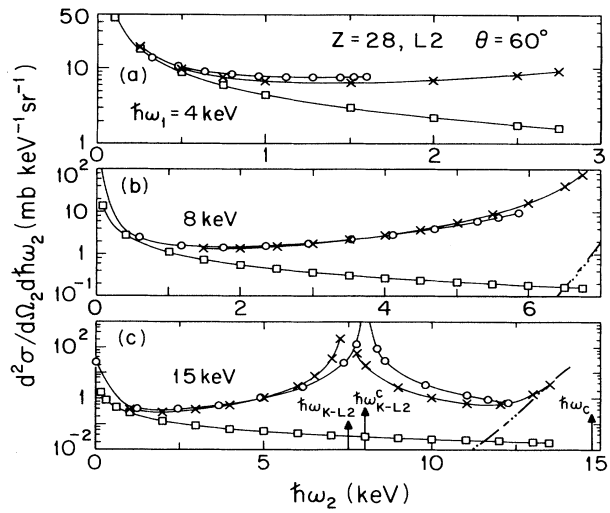

FIG. 21. Same as Fig. 20 except for a scattering angle of 60°. The energy for Compton scattering by free electrons is given by a vertical arrow.

scattering angle. However, the hard-photon end of this spectrum does change as the Compton peak becomes more significant. The peak is the dominant character at this end and is adequately given by the IA and the RIA. We note that the flattening of the peak, predicted by IA for other subshells, does not occur in this case as the $2P$ wave functions are nodeless. We have also calculated the $L3$ contribution to the L-shell cross sections at these same photon energies and scattering angles. The spectra are very similar to the $L2$ spectra and they are not given here. This is expected as, within a nonrelativistic framework, they should be identical. In a relativistic calculation, only minor changes are expected for this intermediate Z case.

We now investigate the scattering of very high-energy photons from the L shell of a high-Z element. In particu-

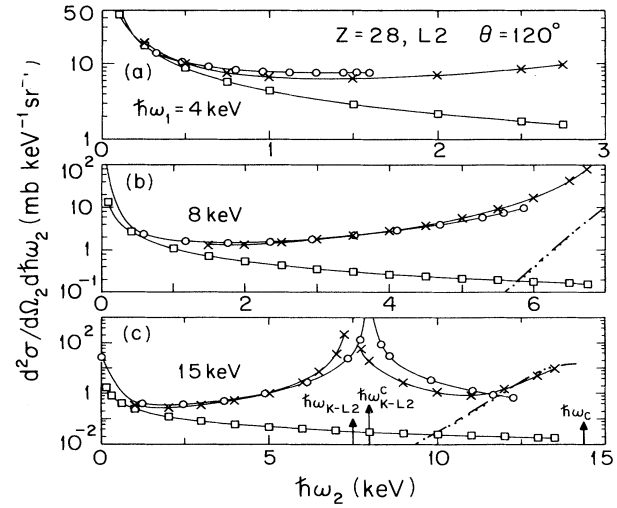

FIG. 22. Same as Fig. 21 except for a scattering angle of 120°.

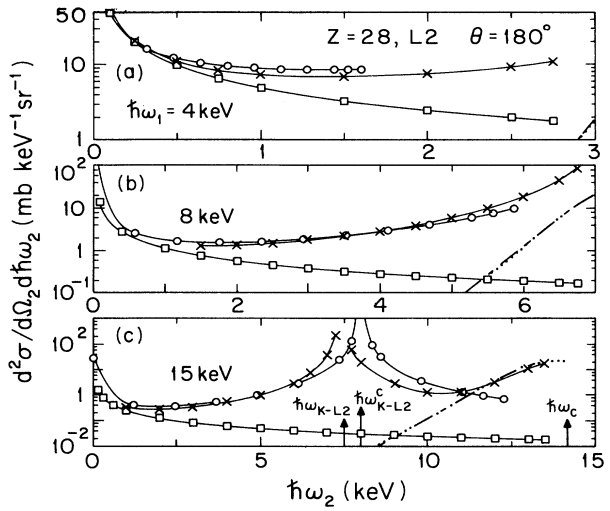

FIG. 23. Same as Fig. 21 except for a scattering angle of 180°.

lar, we consider the scattering of 279.1-keV photons from the $L1$ subshell of Pb in Fig. 24. In this case the resonance at the K-$L1$ transition energy is evident; it is indicated by an arrow. As expected, for the forward-scattering cross section the peak is not completely kinematically allowed. However the onset of the peak makes a contribution comparable to that of the divergent LET terms over a broad range of scattered photon energies. Comparison of the $L1$-subshell peak with the corresponding K-shell peak of Fig. 5 shows that the peak has narrowed and become significantly higher, corresponding to the smaller average momentum of the $L1$ subshell.

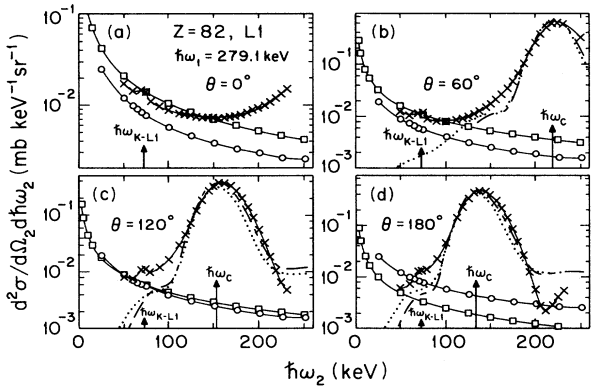

FIG. 24. Doubly differential cross sections for the scattering of 279.1-keV photons from an $L1$ subshell electron of lead into (a) 0°, (b) 60°, (c) 120°, (d) 180°. The cross sections shown are obtained from the nonrelativistic impulse approximation [45] (dotted line), the relativistic impulse approximation [30] (chain-dashed line), the results of the nonrelativistic $\mathbf{p}\cdot\mathbf{A}$ calculations of Gavrila and Tugulea [33] (circles), results obtained from photoeffect cross sections using the low-energy theorem in a screened potential (boxes), and the results of the present S-matrix calculations ($\times$). The energy for Compton scattering by free electrons is shown by the vertical arrow. The data are shown on a logarithmic scale for better presentation of the narrow K-$L1$ resonance (indicated by vertical arrow) and secondary maxima, due to nodal structure in the $L1$ subshell.

The higher kinematic limit for L-shell scattering and the substantial shift of the peak maximum enables one to observe the entire peak for most angles. Agreement of the IA and RIA results with our S-matrix calculations is excellent, although as in the K shell, the IA results are somewhat smaller for back angles. Here we also see, in the spectrum at 180°, the appearance of secondary maxima above (but not below) the peak due to the nodal structure of the $L1$ state.

The corresponding doubly differential cross sections for the $L2$ subshell are given in Fig. 25. The low-energy rise is confined to very low energies and is not very large in magnitude. The resonance at the K-$L2$ transition energy dominates the center of the spectrum at all angles and clearly dominates the K-$L1$ resonance in the L-shell cross section. The nonrelativistic $\mathbf{p}\cdot\mathbf{A}$ results of Gavrila and co-workers [33] accurately predict the low-energy behavior and the resonance behavior, although the resonance is shifted somewhat due to differences in the transition energies of the different atomic models. For finite angles, the Compton peak dominates the high-energy end of the spectrum. This peak is broader than in the $L1$ case. The agreement of the IA and the RIA with the S-matrix results is reasonable, although the IA is somewhat smaller at intermediate angles. For backward scattering, the Compton peak has shifted enough to interfere slightly with the resonance structure.

In calculating the singly differential cross sections for the L subshells, we considered only the previous $L1$ case where some agreement with the RIA results is possible. We do not show the curves here. The cutoffs which we used in our calculations were the K-shell photoionization threshold and 1% of the incident photon energy. In the S-matrix results we neglected the narrow K-$L1$ reso-

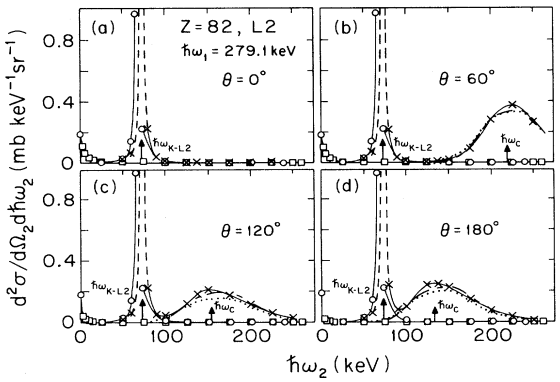

FIG. 25. Doubly differential cross sections for the scattering of 279.1-keV photons from an $L2$ subshell electron of lead into (a) 0°, (b) 60°, (c) 120°, (d) 180°. The cross sections shown are obtained from the nonrelativistic impulse approximation [45] (dotted line), the relativistic impulse approximation [30] (chain-dashed line), the results of the nonrelativistic $\mathbf{p}\cdot\mathbf{A}$ calculations of Gavrila and Tugulea [33] (circles), results obtained from photoeffect cross sections using the low-energy theorem in a screened potential (boxes), and the results of the present S-matrix calculations ($\times$). The energy for Compton scattering by free electrons is shown by the vertical arrow as is the energy of the K-$L2$ transition.

nance. The detailed agreement of the S-matrix results with the RIA was also reflected in the singly differential cross section; the principal differences occurred at small scattering angles. The S-matrix result was nonzero for forward scattering, reflecting the contribution of the soft-photon rise in the spectrum. This contribution was small, however, and so there were only small differences between the S-matrix results, despite large differences in the cutoff energy. The cross section rose above the free photon case, reflecting the infrared rise for soft photons seen with a lower-energy cutoff.

Our calculations of L-shell Compton scattering cross sections have made clear the variety of features in the L shell. For the $L1$ subshell, the doubly differential cross section may exhibit weak resonances, infrared behavior, and the Compton peak. For scattering of photons below the K-shell ionization threshold, the spectrum will be dominated by the soft-photon rise. For energies above the K-shell threshold, the Compton peak region becomes more prominent. We have been able to observe secondary peaks predicted in the $L1$ doubly differential cross sections by more approximate calculations. In the $L2$ and $L3$ subshells, resonant behavior may be important. The resonances occur at the K-$L2$ or K-$L3$ transition energy and dominate the spectrum for incident photon energies just below the K edge. For incident photon energies far below these transition energies, some evidence of the resonances remains observable at the hard-photon end of the spectrum, although the spectrum is dominated by the soft-photon rise. For incident photon energies above the K edge, all three spectral features may be observed in the L subshell spectra.

We now discuss the characteristics of outer-shell cross sections and methods for calculating whole-atom cross sections. The principal issues of concern are how the outer-shell cross sections differ from the inner-shell cross sections that we have already discussed, which approximations are adequate in the outer shells, and which shells require an S-matrix treatment.

All three spectral features occur in outer-shell spectra. For incident photon energies above the K-shell photoionization threshold, resonances occur at the K-X, L-X, M-X, . . . transition energies, if X is the scattering subshell above the K, L, M, . . . subshells. The K-X threshold occurs near the K-L resonance energy, broadening it on the high-energy side. All other resonances occur at significantly lower energies.

The soft-photon energy divergence exists in all outer subshells. The contribution of outer shells in this low-energy region is small. This may be understood in terms of the low-energy theorem. For incident photon energies above inner-shell thresholds, the dominant shell contribution for atomic photoeffect is the shell with the ionization threshold closest to the incident photon energy. Because the Compton matrix element is proportional to the photoeffect matrix element in this low-energy regime, the ratio of the photoeffect cross sections for different shells serves as a rough guide to their contribution to the Compton cross section for soft-scattered-photon energies. We demonstrate this in Fig. 26. Here the low-energy regime for the scattering of 2.94-keV photons from the

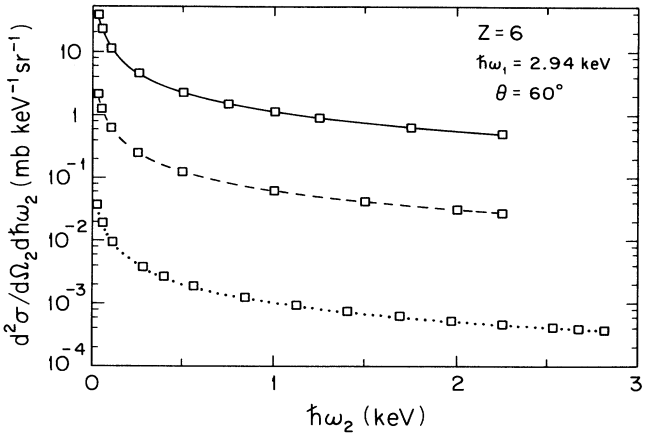

FIG. 26. Comparison of Compton scattering doubly differential cross sections obtained from photoeffect angular distributions using the low-energy theorem for the scattering of 2.94-keV photons from an electron bound in the K shell (solid line), the $L1$ subshell (dashed line), and the $L2$ subshell (dotted line).

electrons of carbon is given for a scattering angle of 60°. The ratio of the subshell contributions is in rough agreement with the total screened photoeffect cross sections of Scofield [63], who gives a K to $L1$ ratio of 20 and a K to $L2$ ratio of 1250 for 3-keV incident photons. Clearly the K-shell contribution is dominant and is a good approximation to the whole-atom result.

In Fig. 27, we give the doubly differential cross sections for the scattering of 2.94-keV photons from all of the electrons in a carbon atom. Most of the spectrum is dominated by the low-energy behavior corresponding to the K-shell $\mathbf{p}\cdot\mathbf{A}$ terms. The resonances which were prominent at 0.28 keV in the $L2$ subshell cross sections are barely visible here. The peak occurs only at the

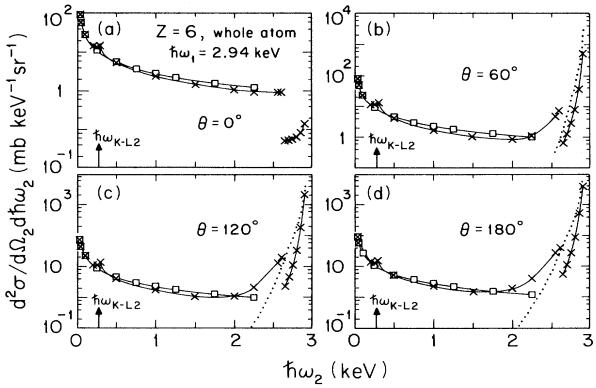

FIG. 27. Doubly differential cross sections for the scattering of 2.94-keV photons from all of the electrons of a carbon atom into (a) 0°, (b) 60°, (c) 120°, (d) 180°. We show impulse approximation results [45] (dotted line), the S-matrix calculations of this work ($\times$), and results for K-shell electrons obtained from photoeffect angular distributions using the low-energy theorem (boxes). The energy for the characteristic K-L transition is indicated by the vertical arrow.

hard-photon end of the spectrum. In the peak region, the IA results are adequate. However, the IA results used here are based on whole-atom Compton profiles. These Compton profiles are functions of momentum transfer only and cannot model effects associated with electron binding. At 2.6 keV there is a break in the whole-atom cross section due to the K-shell kinematic limit. This limit is not adequately modeled in the IA based on the whole-atom Compton profiles.

In Fig. 28 we give the scattering cross sections for 279-keV photons scattered from lead calculated in the IA IA and the RIA. Superimposed on these results are the K- and L-shell cross sections. Clearly the low-energy spectrum is dominated by the inner-shell contributions. However, as expected, the contributions of the inner shells are negligible in the peak region. Differences between the IA and the RIA calculations exist for hard photons where the RIA predicts a step structure that is not given by the IA. Again this is due to the fact that the IA calculations were obtained from whole-atom data, neglecting kinematic limits, whereas the RIA calculations were obtained by summing subshell results which took kinematic limits into account.

The low-energy regime in total atom scattering, and the entire spectrum for forward scattering, is given by resonances superimposed on the low-energy rise of the innermost scattering state. For higher scattered photon energies, the peak region is dominant. The behavior of outer subshells in this region is quite different than the inner-shell shape. The average momentum in the inner shells is much larger than in the outer shells, causing the inner-shell profiles to be broader and smaller in magnitude than the outer-shell results. Therefore, the center of the peak is given primarily by the outer subshell cross section, whereas the width of the peak is given by the inner shells. The outer-shell cross sections are adequately given by the RIA or IA results at the energies considered here. Impulse approximation calculations obtained using whole-atom momentum distributions may be in error due to neglect of kinematic limits. This problem in calculating whole-atom IA results may be remedied by summing the correct subshell cross sections rather than using whole-atom momentum distributions.

For most practical applications (incident photon energy above the K-shell ionization threshold and scattered photon energies above the resonant region), the cross section singly differential in scattered photon angle will be dominated by the peak region contributions of the outer shells and so the effects discussed here will not be significant. For forward angles, electron binding is manifested principally by the need to impose kinematic limits on the doubly differential cross sections of individual subshells. These kinematic limits are not reflected in tabulations of the integrated whole-atom incoherent scattering factors as simple functions of momentum transfer and, hence, modifications to the incoherent scattering factor should be necessary for this regime of small momentum transfer. For incident photon energies below the K-shell ionization threshold, substantial corrections to the incoherent scattering factor may be necessary to reflect the dominant resonant behavior of one or more inner subshells.

In Fig. 29 we investigate the effects of the divergent contribution of the $\mathbf{p}\cdot\mathbf{A}$ term on the total incoherent scattering cross section for the hydrogen atom, assuming a 10-eV cutoff in scattered photon energy. The same cutoff was taken both for radiative corrections to photoeffect and for Compton scattering. Results are, of course, independent of the energy of the cutoff. We see that, although in the hydrogen atom the $\mathbf{p}\cdot\mathbf{A}$ terms dom-

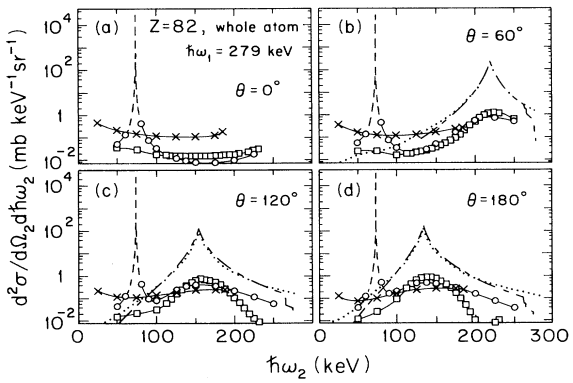

FIG. 28. Doubly differential cross sections for the scattering of 279-keV photons from all of the electrons of a lead atom into (a) 0°, (b) 60°, (c) 120°, (d) 180°. We show whole-atom doubly differential cross sections calculated in the impulse approximation [45] (dotted line) and the relativistic impulse approximation [30] (chain-dashed line). Superimposed on these whole-atom results are the S-matrix predictions of the present work for the K shell ($\times$), for the $L1$ subshell (boxes), and for the $L2$ subshell (circles). The difference in the Compton peak region demonstrates the importance of scattering from outer-shell electrons.

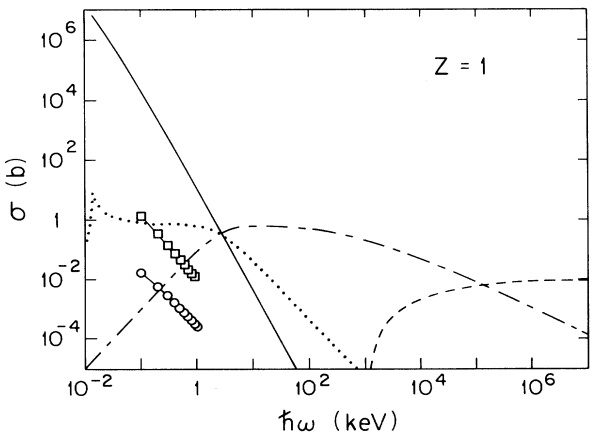

FIG. 29. Photon-atom interaction cross section for H. Shown are the magnitude of the radiative corrections to photoeffect [53,64] (boxes) and the contribution of the $\mathbf{p}\cdot\mathbf{A}$ terms of the nonrelativistic Hamiltonian to the total Compton scattering cross section [32] (circles), for incident photon energies above 100 eV. Also shown are total cross section for photoeffect (solid line), elastic scattering (dotted line), incoherent scattering (chain dashed line) from the incoherent scattering factor, and pair production (dashed line) (taken from Ref. [65]), for incident photon energies above 10 eV.

inate the Compton cross section to a relatively high ratio of incident photon energy to electron binding energy, these contributions are negligible compared to the photoeffect and even to the radiative corrections to the photoeffect in the total photon-atom interaction cross section. Note however that the total Compton cross section does not continue to fall at low energies in the way that the incoherent scattering factor would predict.

III. COMPARISON WITH EXPERIMENT

In this section we compare cross sections, calculated within the formalism presented above, with values measured in several recent experiments [5–9,55], typical of work performed in this field. As has been mentioned, experiments on inelastic scattering of photons have been performed for many years and there are a number of different types of experiments. While recent experiments [10] detecting both the ejected electron and the scattered photon are expected to be quite useful as diagnostic tools for target electron momentum density, we do not discuss these results, as the available data is generally in regions well described by the impulse approximation. We concentrate instead on experiments where the scattered photon, and perhaps a fluorescence photon, is detected. If the fluorescence photon is detected, the scattering subshell can be determined. If it is not, then the scattering occurs from any electron in the atom.

Four of the experiments discussed here are recent examples of coincidence experiments where the doubly differential cross section for scattering of photons from the K shell is measured. Two of these experiments are rather typical of much of the work in this field; here high-energy nuclear sources of unpolarized radiation were used for scattering from the K shell of high-Z elements [8,55]. The other two experiments were performed at much lower energies, using either a nuclear source or radiation from a synchrotron which was prepared in a high degree of linear polarization, on elements of intermediate Z, in order to examine the validity of the impulse approximation at intermediate momentum transfer [5,7]. Additional experiments in the coincidence mode have been performed for the L shell [66]. We do not discuss these experiments here as they have been performed where the impulse approximation is adequate. In the case where only the direction of the scattered photon is observed in coincidence with the fluorescence photon, we discuss the K-shell experiment of Wolff *et al.* [9], which shows surprising agreement with Whittingham's integrated cross section [11].

There have been a number of experiments performed in which the fluorescence photon is not detected. These experiments include results for the doubly differential cross section for the whole atom, but more often only the direction of the scattered photon is detected, yielding the incoherent-scattering factor. For the doubly differential cross section we have already presented comparison with whole-atom scattering experiments at photon energies above the K edge [3]. We have seen, in these cases, that inner-shell contributions (which must be calculated using the S matrix) are important mainly in the soft-photon region of the spectrum, where experimental data is not available, and they contribute negligibly in the peak region of the spectrum. Here we discuss the experiment of Briand *et al.* [6], which was performed below the K-shell binding energy in an attempt to detect the contribution in the infrared and resonant regions from the L shell. We discuss the contributions of the higher shells in this case.

We do not present data for the whole-atom incoherent-scattering factor, defined to be the contribution from the peak terms of the doubly differential cross section. As discussed above, the inner-shell contributions of concern here are only important away from the Compton peak.

We discuss the results of the various experiments in light of our exact calculations. In all of the results presented below, our calculations use potentials and wave functions obtained with the relativistic self-consistent-field method. These IPA potentials should be adequate for our purposes, where we are mainly interested in descriptions of inner-shell states, as they have been adequate in calculations of Rayleigh scattering [15] and photoeffect [63] for these shells at these energies. (At lower energies and for outer shells correlation effects should be included.) We use the same DFS potentials and wave functions for results obtained from the photoeffect differential cross section, with the low-energy theorem, and in calculations in the RIA. Thus for a given potential, we can see the importance of the different levels of approximation. In the situations considered, screening effects do matter.

We first discuss traditional coincidence measurements using relatively high-energy nuclear sources. At these energies one must scatter from high-Z elements in order to observe any deviation from impulse approximation [2]. The K-shell contribution to the total Compton cross section is very small and, coupled with an isotropic source which is not very intense, results in poor counting statistics. In Figs. 30(a) and 30(b) we compare the results of the measurements of Basavaraju, Kane, and George [55] for the scattering of 279-keV photons from the K shell of tin into 90° and 115° with the nonrelativistic form factor [24], the IA [45], the RIA [30], and the S-matrix calculations of the present work. The experimental data is unable to distinguish between the theories, even in the peak region where substantial differences between calculations exists. In a subsequent study [8] the authors reported errors in their method of data analysis, affecting the spectrum in the infrared and peak regimes. While they did not report corrected values for the measurements just discussed, the authors did present data for the scattering of 320-keV photons from the K shell of holmium into 45° and 115° and for gold into 115°. The results of comparisons between our S-matrix results and these improved measurements for holmium have been reported elsewhere [1]. In Fig. 30(c) we compare these recent measurements for the Compton doubly differential cross section of gold with our S-matrix results. Also shown are IA [45] and RIA [30] calculations and the form-factor results of Schnaidt [24]. As in the previous study, although the theoretical approaches differ the experimental values show no systematic agreement with theory. Additionally,

the experimental uncertainties (due to poor counting statistics) are larger than the substantial differences between the theoretical values. In the infrared region the situation is worse as the large number of electrons which may ionize can produce false coincidences via bremsstrahlung emission.

Manninen, Hämäläinen, and Graeffe [7] performed an experiment with a source of low-energy (59.54 keV) photons scattered from copper and zirconium through angles $\Theta=125°$ and $\Theta=128°$. Their intention was to provide a test for the validity of impulse approximation in the low-momentum-transfer region. Although they did not expect good agreement with the impulse approximation (since $ka_0=0.94$ for copper and $ka_0=0.67$ for zirconium and, as was discussed in the Introduction, the usual criterion for the validity of the IA has been $ka_0 \gg 1$), they reported that the impulse approximation explains the spectral shape surprisingly well. Their measurement was not absolute, but was normalized to theoretical values in the peak region. They estimated bremsstrahlung by assuming negligible Compton scattering contributions below approximately 20 keV and that the bremsstrahlung contribution be zero at the kinematic limit for K-shell scattering. Measured spectra were presented for energies above 20 keV. In Fig. 31(a) we present the criterion (10) and in Fig. 31(b) we give the comparison of our calculation with Manninen's experiment for the K shell of copper, shown on an absolute scale with their data normalized to the IA values. We also present the corresponding IA results for this case. Our results confirm their conclusion that, as below in the experiment of Marchetti and Franck on this same element for a similar energy [5], the impulse approximation is satisfactory, as would be expected from criterion (10) [shown in Fig. 31(a)]. This point has been discussed in detail in Ref. [2]. We can also confirm the authors' assumption that near 20 keV there is no noticeable Compton contribution.

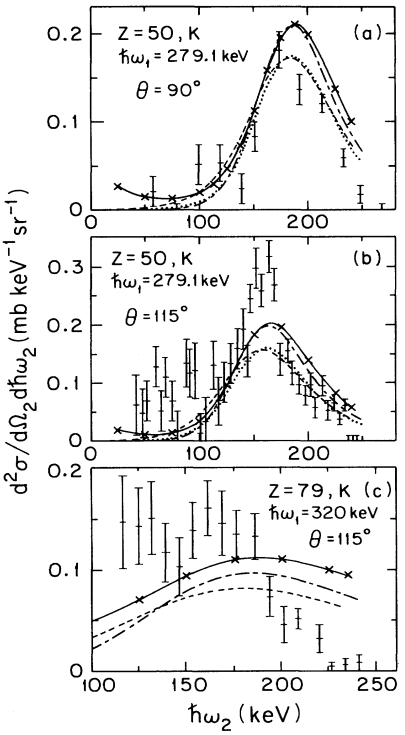

FIG. 30. (a) Comparison of our S-matrix calculations ($\times$) for the scattering of 279.1-keV photons from a K-shell electron of tin into 90° with the experiment of Basavaraju, Kane, and George [55] (points with error bars). Other symbols are as in Fig. 3. (b) Same as (a) except for 115°. (c) Same as (b) except for 320-keV photons from a K-shell electron in gold. The experimental data are from Ref. [8].

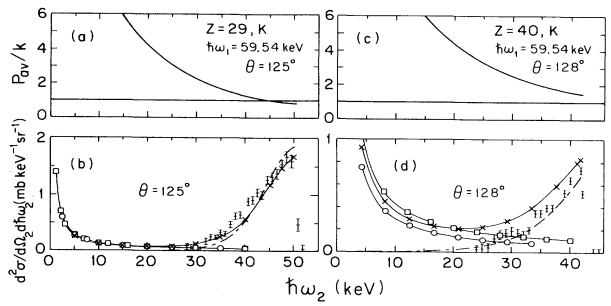

FIG. 31. Scattering of 59.54-keV photons from the K shell of copper into 125°. (a) The measure of validity of the impulse approximation [Eq. (10)]. (b) Comparison of the experimental data of Manninen, Hämäläinen, and Graeffe [7] (points with error bars) with our S-matrix calculations ($\times$). Also shown are Gavrila's $\mathbf{p}\cdot\mathbf{A}$ results [32] (circles) and the relativistic impulse approximation results [30] (chain-dashed line). (c) and (d) Same as (a) and (b) except for the scattering of 59.54-keV photons from the K shell of zirconium into 128°.

In Figs. 31(c) and 31(d) we present, along with the criterion for the validity of IA [Eq. (10)], the comparison of our calculation with the zirconium experimental results in the high-energy part of the spectrum. As already mentioned, the authors did not expect to get agreement with the IA because of the small momentum transfer ($ka_0=0.67$). To their surprise, they found very good agreement with the impulse approximation. Our calculation shows similar behavior at the high-energy end of the spectrum to that predicted by IA. However it also shows that there is no region where the Compton contribution can be neglected as the authors assumed when estimating bremsstrahlung. Below 20 keV, the Compton differential cross section rises as the scattered photon energy decreases. At 20 keV the Compton cross section is about 25% of the maximum value (at the hard-photon end). Our calculation shows very good agreement at the soft-photon end of the spectrum with more approximate calculations (Gavrila's $\mathbf{p}\cdot\mathbf{A}$ approximation and the low-energy formula). At the hard-photon end it approaches the impulse approximation as the criterion [shown in Fig. 31(c)] predicts. Based on our calculations, we suggest that the authors have subtracted significant Compton contributions together with the bremsstrahlung contribution (at their 20-keV point). Although it was not the author's intention to observe the infrared divergent behavior in the Compton spectrum, and they did not observe photons below 20 keV, we believe that the achieved experimental accuracy in their measurement could make it possible to observe this interesting behavior at 20 keV,

if this accuracy could be attained in an absolute measurement and if an independent estimate of secondary bremsstrahlung could be made.

The availability of synchrotron-radiation sources now makes it possible to perform experiments in all regions of the Compton spectrum [4]. The high-photon fluxes increase the counting statistics, decreasing the experimental uncertainties, thus enabling one to better distinguish between different theories. The advantages of using synchrotron radiation in the resonant Raman and the infrared regions also includes the relatively low energies available, the tunability of the source, and the possibility to make use of the polarization properties of the photon beam in order to minimize contributions of the A^2 term in the KHW matrix element [4].

Recently, Marchetti and Franck [5] have reported a series of measurements of the scattering of 62- and 70-keV photons from the K shell of copper. They reported reasonable agreement with a numerical evaluation of the A^2 term of the KHW matrix element, using screened wave functions. In Fig. 32 we present a comparison of their experimental data for the scattering of 70-keV photons from the K-shell electrons of copper into 90° with our S-matrix results. The agreement between theory and experiment is good, although despite the fact that the counting statistics in this case are the best reported by these authors, the error bars are substantial and it should be noted that there is an uncertainty of 15% in normalizing the experimental data [5]. Estimates of the $\mathbf{p}\cdot\mathbf{A}$ contributions were also given as well as a very complete analysis of secondary processes leading to false coincidences. We have confirmed the conclusion, in this case, that the spectrum in the low-energy region is much smaller than the authors' estimate of photoelectron bremsstrahlung generated false coincidence counts.

A very recent experiment of Briand *et al.* [6] attempted to exploit the characteristics of synchrotron radiation discussed above in a noncoincidence measurement performed on zirconium, using a linearly polarized synchrotron source at energies ranging between 14 and 17.4 keV (the largest energy used is slightly below the K-shell binding energy for this element). Photons were collected parallel to the incident photon polarization vector, assuring that the A^2 term of the KWH matrix element would not contribute. As has been explained, this is a resonant region for Compton scattering and, as predicted by Gavrila, resonances occur for energies corresponding to fluorescent lines. The resonant behavior which corresponds to the K-L resonance was observed at the high-energy end of the spectrum. The resonance at its maximum was not observed because the incident photon energy was below the K-shell binding energy. The observed resonant behavior was strongest at the highest applied energy (17.4 keV). Scattered photons of all energies higher than approximately 2 keV (which corresponds to the highest L-M resonant energy) were detected. At the low-energy end of the spectrum, a large number of soft photons were observed. Since this was not a coincidence measurement there were contributions from all energetically allowed, occupied shells of the atom. The authors argued that the contribution of the shells less tightly bound than the L shell to the Compton scattering should not be significant as the infrared behavior is strongest for the innermost energetically allowed shell. This may be readily seen from the total photoeffect cross sections of Scofield [63], which are much larger at this energy for the L shell than for the M shell. The authors ascribed the low-energy photons to the infrared divergence of the Compton spectrum from L-shell electrons, a rise in the spectrum stronger than theoretically predicted by roughly an order of magnitude. They claimed to have corrected for bremsstrahlung, but some doubts persist [67]. We present results for this case including calculations for the L and M shells. We include the M shell because the contributions of all shells should be considered and, although the M-shell infrared behavior is smaller than that of the L shell in this regime, there are L-M resonances expected where the excess photons were observed. In Fig. 33(a) we compare our L-shell contributions with the experimental data for the scattering of 14-keV photons. Clearly the L-shell predictions do not adequately describe the experimental data. In Fig. 33(b) we include the M-shell contribution in our calculations for this case. Due to the fact that there are several resonances, we only show the spectrum to the onset of this regime. We observe that contrary to the assumptions of the authors, the M shell begins to dominate in this region due to the L-M resonances. We also came to this conclusion in the highest-energy case (17.4 keV) considered by the authors.

Finally, in Fig. 34, we compare the experimental results of Wolff *et al.* [9] for the singly differential (in scattered photon angle) photon scattering cross section for the K shell for scattering of 661.6-keV photons from lead with our S-matrix results and with the results of Whittingham. In the S-matrix calculations, a low-energy photon cutoff must be assumed in order to define this cross section. In the calculations of Whittingham this corresponds to an energy of approximately 100 keV. We chose the experimental cutoff (103 keV) in order to facilitate comparison, and we also tried a cutoff of 6 keV in order

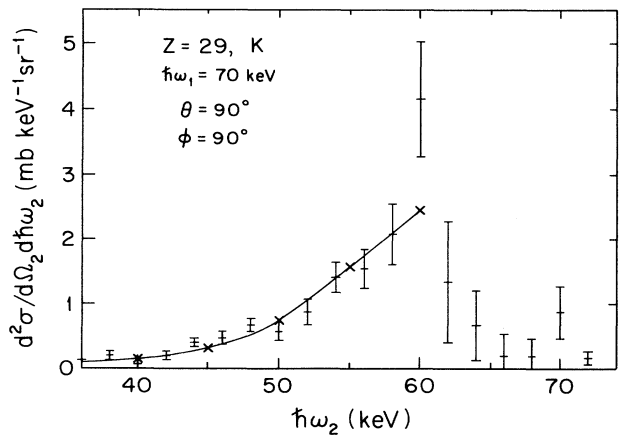

FIG. 32. Comparison of the experimental data of Marchetti and Franck [5] (points with error bars) for the scattering of 70-keV linearly polarized photons (polarization vector perpendicular to plane defined by incident and scattered photon momenta) from the K shell of copper into 90° with our S-matrix calculations (×).

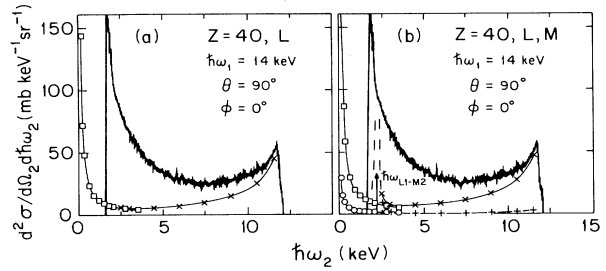

FIG. 33. (a) Comparison of the resonant experiment of Briand *et al.* [6] (experimental curve) with our S-matrix ($\times$) and low-energy theorem calculations (boxes) for the L-shell contributions for the scattering of 14-keV photons from all of the electrons of a zirconium target into 90°. Here the incident photon beam is linearly polarized in the plane defined by the incident and scattered photon momenta. The vertical line below 2 keV represents the experimental cutoff. (b) Same as (a) except shown are theoretical M-shell contributions [S-matrix calculation (+), low-energy theorem calculations (circles)] and $L+M$ contributions [S-matrix calculation ($\times$), low-energy theorem calculations (boxes)]. The L-M resonant region is indicated by dashed lines. Only the energy for the characteristic $L1$-$M2$ transition is shown by the vertical arrow. All M-shell contributions are included in our calculation.

to investigate the effects of retaining divergent low-energy contributions. We also show the results based on integrating the relativistic impulse approximation calculations. For forward angles, the experimental values do not agree systematically with any theory. At these angles the contributions of the $\mathbf{p}\cdot\mathbf{A}$ terms may be significant. This is especially evident for forward scattering where, as seen in Fig. 9(a), the doubly differential cross section is completely given by these terms, yielding a nonzero scattering factor. For intermediate scattering angles, the S-matrix results with the cutoff taken near the experimental cutoff, both Whittingham's and ours, agree reasonably well with experiment. The experimental values agree only with Whittingham's results for back angles, where a large drop occurs. In Fig. 9(d) we show, for a scattering angle of 180°, that this discrepancy cannot be explained by the $\mathbf{p}\cdot\mathbf{A}$ contribution. At this angle, and for most back angles, the contribution of this term is small and the doubly differential cross section is dominated by the peak, where excellent agreement between our results and the RIA is evident. Whittingham did not present data at this angle. However, as was seen in Fig. 7, his result is significantly smaller than both the RIA and our calculation for back angles. He suggested that this drop at back angles in his singly differential cross section might be in error [11].

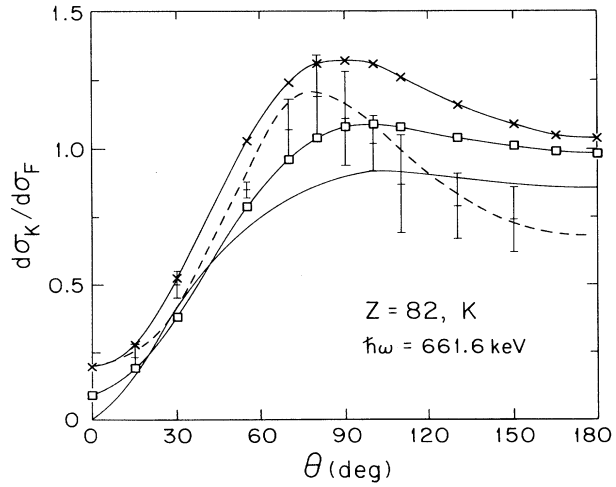

FIG. 34. K-shell scattering factors for the scattering of 661.6-keV photons from the K shell of lead. Shown here are our S-matrix calculations with low-energy cutoffs of 6 keV ($\times$), 103 keV (boxes). Also shown are the S-matrix results of Whittingham [11] (dashed line), the relativistic impulse approximation [29] (solid line), and the experimental data of Wolff *et al.* [9].

IV. CONCLUSIONS

We have presented an *ab initio* method for calculating Compton scattering spectra, based on the numerical solution of the relativistic second-order external field QED S-matrix element for this process in the independent-particle approximation. This method predicts the observed spectral features in the infrared region, in the peak region, and in the resonant regime. This type of approach is necessary primarily for evaluating inner-shell amplitudes, particularly in regimes where these spectral features overlap and where no single simpler approximate method adequately gives the spectrum. We have systematically investigated inner-shell cross sections. An initial assessment of the validity of widely used approximate methods has been given. We find that the use of the relativistic impulse approximation [30] in conjunction with the low-energy theorem adequately reproduces the spectrum in many cases of physical interest. For the K shell we confirm the limited earlier work of Wittwer [12], but not the more widely quoted results of Whittingham [11].

We have discussed the extension of our results to outer atomic subshells, performing S-matrix calculations for all atomic electrons at low incident photon energies and examining the use of approximate methods in the outer shells at higher photon energies. In these cases we find significant low scattered photon energy structure, infrared and resonant, in our S-matrix calculations, not predicted by the usual impulse approximation results, but understood in terms of the nonrelativistic $\mathbf{p}\cdot\mathbf{A}$ matrix element. We also observe structures, in the Compton peak region of our calculations, both due to the nodal structure of the electron state (seen above the peak) and due to kinematical limits of contributing subshells. The latter are not predicted in tables of whole-atom Compton profiles, but may be obtained in IA calculations performed separately for each subshell. We have integrated our cross sections over scattered photon energy, assuming reasonable low-energy cutoffs, in order to obtain the cross section singly differential in scattered photon angle. Here we find significant departures from the incoherent-scattering factor results, particularly at low incident photon energies for the K shell of light elements.

We confirm that recent experiments at 60–70 keV [5,7]

on the K shell of copper are adequately described by theories which use only the A^2 term of the KHW matrix element. We have found, in contrast to the authors' analysis, that a corresponding recent experiment on the K shell of zirconium [7] was not adequately described by the impulse approximation. We present more detailed calculations in the recent, controversial experiment of Briand *et al.* [6]. Our calculations include significant resonant contributions from the M shell, which were neglected by the authors. We have discussed the problem of experimentally observing the infrared divergence predicted by the low-energy theorem, earlier nonrelativistic Coulombic calculations, and within the present formalism.

ACKNOWLEDGMENTS

This work was performed under NSF Grants No. PHY8704088, No. PHY9005763, No. INT8704953, and No. JFPPP767. One of us (T.S.) would like to thank the Open Society Fund (for Croatia) for travel funding. Some of the calculations presented here were performed on CRAY Y-MP, on Connection Machine CM-5, and on DEC-RISC supercluster computers at the Pittsburgh Supercomputing Center under Grant No. PHY89015P. We thank Dr. Josef Stein and Mr. David Shaffer for their efforts in making the code run on the CM-5. We also thank Mr. David Shaffer for investigating the radiative corrections to photoeffect. One of us (P.M.B.) would like to thank Mr. Michael Kopko of the PSC for his assistance.

APPENDIX: NOTATION AND DEFINITIONS

We use definitions of Dirac γ matrices and other notations as are in Ref. [68]. The wave function of an electron with energy E, angular momentum j, and orbital angular momentum l can be written in the form [68]

$$\psi^m_{\kappa,E}(\mathbf{r})=\begin{bmatrix} i\dfrac{G_\kappa(r)}{r}\varphi^m_\kappa(\hat{\mathbf{r}}) \\ \dfrac{F_\kappa(r)}{r}\boldsymbol{\sigma}\cdot\hat{\mathbf{r}}\varphi^m_\kappa(\hat{\mathbf{r}}) \end{bmatrix}, \qquad \kappa=\begin{cases} -(j+1/2), & l<j \\ (j+1/2), & l>j \end{cases} \tag{A1}$$

where σ_x, σ_y, and σ_z are Pauli 2×2 spin matrices. The two component spinors φ^m_κ are given by

$$\varphi^m_k(\hat{\mathbf{r}})=(-1)^{j-m}(2j+1)^{1/2}\begin{bmatrix} \begin{pmatrix} l & \frac{1}{2} & j \\ m-1/2 & \frac{1}{2} & -m \end{pmatrix} Y_l^{m-1/2}(\hat{\mathbf{r}}) \\ \begin{pmatrix} l & \frac{1}{2} & j \\ m+1/2 & -\frac{1}{2} & -m \end{pmatrix} Y_l^{m+1/2}(\hat{\mathbf{r}}) \end{bmatrix}. \tag{A2}$$

The Y_l^m are spherical harmonics and the objects in parentheses are 3-j coefficients defined as in Ref. [69]. The radial functions G_κ and F_κ satisfy the coupled homogeneous differential equation

$$\frac{dG_\kappa}{dr}+\frac{\kappa}{r}G_\kappa-[1+E-V(r)]F_\kappa=0\ , \qquad \frac{dF_\kappa}{dr}-\frac{\kappa}{r}F_\kappa-[1-E+V(r)]G_\kappa=0\ . \tag{A3}$$

For energies $E>1$ the solutions are oscillatory functions and, for $E<1$, the bound like solutions are exponentially decreasing functions as $r\to\infty$, except for energies in the negative-energy continuum, which behave in an oscillatory fashion. In both cases the boundary conditions are imposed by requiring quadratic integrability for the solution [68].

The wave function of an outgoing electron of asymptotic momentum p and spin projection α is the solution of the coupled equations which far from the origin behaves as the sum of the appropriate distorted plane wave and a distorted incoming spherical wave. The partial-wave expansion of this function is [70]

$$\psi_e(\mathbf{r})=\frac{1}{\sqrt{pE}}\sum_{\kappa,m}(i)^{l-1}(\varphi^{m\ +}_\kappa(\hat{\mathbf{p}})\varphi_s)e^{-i\delta_\kappa}\psi^m_{\kappa,E}(\mathbf{r})\ , \tag{A4}$$

where $\psi^m_{\kappa,E}$ is given by Eq. (A1), δ_κ denotes the partial-wave phase shift, E denotes energy, $\mathbf{p}$ is the momentum, and φ_s represents spin states:

$$\varphi_{1/2}=\begin{bmatrix}1\\0\end{bmatrix},\quad \varphi_{-1/2}=\begin{bmatrix}0\\1\end{bmatrix}.$$

The wave functions $\psi_e=\psi_{\mathbf{p},s}$ for the electron scattering states are normalized as

$$\int\psi^+_{\mathbf{p},s}\cdot(\mathbf{r})\psi_{\mathbf{p}',s}\cdot(\mathbf{r})d^3r=\delta_{s,s'}\delta^3(\mathbf{p}-\mathbf{p}')\ . \tag{A5}$$

The bound-electron wave functions are normalized to unity.

The photon plane-wave function used in our calculations is

$$\mathbf{A}(\mathbf{x})=\frac{1}{\sqrt{2\omega}(2\pi)^{3/2}}\boldsymbol{\epsilon}e^{i\mathbf{k}\cdot\mathbf{x}},\quad \omega=|\mathbf{k}|\ , \tag{A6}$$

where $\boldsymbol{\epsilon}$ denotes the polarization and $\mathbf{k}$ the momentum of the photon. For this wave we have used the multipole expansion [70]

$$\boldsymbol{\epsilon}e^{i\mathbf{k}\cdot\mathbf{x}}=4\pi\sum_{L,M,\lambda}(i)^{L-\lambda}[\boldsymbol{\epsilon}\cdot\mathbf{Y}^{(\lambda)*}_{L,M}(\hat{\mathbf{k}})]\cdot\mathbf{a}^{(\lambda)}_{L,M}(\mathbf{x},k)\ , \tag{A7}$$

where L, M, and λ denote the angular momentum, the projection of angular momentum, and the parity of the partial wave. The function $\mathbf{a}^{(\lambda)}_{L,M}(\mathbf{x},k)$ is given by

$$\mathbf{a}^{(0)}_{L,M}(\mathbf{x},k)=j_L(kr)\mathbf{Y}^{(0)}_{L,M}(\hat{\mathbf{x}}) ,$$

$$\mathbf{a}^{(1)}_{L,M}(\mathbf{x},k)=\frac{1}{\sqrt{2L+1}}[\sqrt{L+1}\,j_{L-1}(kr)\mathbf{Y}_{L,L-1,M}(\hat{\mathbf{x}}) -\sqrt{L}\,j_{L+1}(kr)\mathbf{Y}_{L,L+1,M}(\hat{\mathbf{x}})] . \tag{A8}$$

The vector spherical harmonics $\mathbf{Y}^{(\lambda)}_{L,M}$ and $\mathbf{Y}_{L,L',M}$ are defined as in Ref. [70].

Using the multipole expansion (A7) of the photon wave we can write the function $F(\mathbf{x},\eta)$ [Eq. (17)] in the form

$$F(\mathbf{x},\eta)=4\pi\sum_{L,M,\lambda}(i)^{L-\lambda}[\boldsymbol{\epsilon}\cdot\boldsymbol{\Psi}^{(\lambda)*}_{L,M}(\hat{\mathbf{k}})]\cdot F^{(\lambda)}_{L,M}(\mathbf{x},\eta) , \tag{A9}$$

where

$$F^{(\lambda)}_{L,M}(\mathbf{x},\eta)=-\int d^3y\, S_v(\mathbf{x},\mathbf{y},\eta)\boldsymbol{\gamma}\cdot\mathbf{a}^{(\lambda)}_{L,M}(\mathbf{y},k)\psi_B(\mathbf{y}) . \tag{A10}$$

Note this is still a function of all final electron spatial variables. The function $F^{(\lambda)}_{L,M}$ satisfies the inhomogeneous Dirac equation

$$[i\nabla\cdot\boldsymbol{\alpha}-\beta-V(r)+\eta]F^{(\lambda)}_{L,M}(\mathbf{x},\eta)=-\boldsymbol{\alpha}\cdot\mathbf{a}^{(\lambda)}_{L,M}(\mathbf{x},k)\psi_B(\mathbf{x}) , \tag{A11a}$$

with boundary conditions determined from the propagator boundary conditions. Namely, for $|\mathbf{x}|=r\to\infty$,

$$F^{(\lambda)}_{L,M}(\mathbf{x},\eta)=\begin{cases}\dfrac{\tilde{F}}{r}e^{i(\eta^2-1)^{1/2}r} & \text{for } |\eta|>1,\\ \dfrac{\tilde{F}_0}{r}e^{(1-\eta^2)^{1/2}r} & \text{for } |\eta|<1 ,\end{cases} \tag{A11b}$$

where $\tilde{F}$ and $\tilde{F}_0$ denote r-independent four-spinor functions as determined by numerical calculations. Far from the origin, the function $F^{(\lambda)}_{L,M}$ should behave as an outgoing spherical wave for $|\eta|>1$. This does not depend on the sign of the energy in the propagator (for the emission-first matrix element η can be negative if $\omega_2>2-E_B$). Equation (A11a), with boundary conditions Eq. (A11b), completely determines the function $F^{(\lambda)}_{L,M}$. This function $F^{(\lambda)}_{L,M}$ can further be expanded in the form

$$F^{(\lambda)}_{L,M}(\mathbf{x},\eta)=\sum_{\kappa_1,m_1}A^{L,M,\lambda}_{\kappa_1,m_1}\begin{bmatrix} i\dfrac{g\kappa_1(r)}{r}\varphi^{m_1}_{\kappa_1}(\hat{\mathbf{r}}) \\ \dfrac{f_{\kappa_1}(r)}{r}\boldsymbol{\sigma}\cdot\hat{\mathbf{r}}\varphi^{m_1}_{k_1}(\hat{\mathbf{r}})\end{bmatrix} . \tag{A12}$$

Making a similar expansion for the inhomogeneous term of Eq. (A11) and taking

$$A^{L,M,\lambda}_{\kappa_1,m_1}=i(-1)^{m_1-1/2}\tfrac{1}{2}[1+(-1)^{(l_1+l_0+L+\lambda+1)}]\times\tfrac{1}{2}\left[\frac{(2j_1+1)(2j_0+1)(2L+1)}{4\pi L(L+1)}\right]^{1/2}\times\begin{bmatrix}j_1 & j_0 & L\\ \frac{1}{2} & -\frac{1}{2} & 0\end{bmatrix}\begin{bmatrix}j_1 & j_0 & L\\ m_1 & -m_0 & M\end{bmatrix} , \tag{A13}$$

the radial functions g_{κ_1} and f_{κ_1} in Eq. (A12) satisfy the coupled inhomogeneous radial equations

$$\frac{dg_{\kappa_1}}{dr}+\frac{\kappa_1}{r}g_{\kappa_1}-[1+\eta-V(r)]f_{\kappa_1}=G_{\kappa_0}\mathcal{H}^{\lambda}_{L,\kappa_0,-\kappa_1} ,$$
$$\frac{df_{\kappa_1}}{dr}-\frac{\kappa_1}{r}f_{\kappa_1}-[1-\eta+V(r)]g_{\kappa_1}=F_{\kappa_0}\mathcal{H}^{\lambda}_{L,-\kappa_0,\kappa_1} . \tag{A14}$$

The functions G_{κ_0} and F_{κ_0} are the bound-electron radial functions as defined in Eq. (A1). The function $\mathcal{H}^{\lambda}_{L,\kappa_0,\kappa_1}$ contains the photon radial wave functions and has the form

$$\mathcal{H}^0_{L,\kappa_0,\kappa_1}(kr)=(\kappa_0-\kappa_1)j_L(kr) ,$$
$$\mathcal{H}^1_{L,\kappa_0,\kappa_1}(kr)=\frac{L+1}{2L+1}(L-\kappa_0-\kappa_1)j_{L-1}(kr) -\frac{L}{2L+1}(L+\kappa_0+\kappa_1+1)j_{L+1}(kr) . \tag{A15}$$

The radial integrals that appear in the expressions for the coefficients $C^{0,2}_J$ of Eq. (23) have the form

$$I^{[e,\gamma]}_a=P^{[e,\gamma]}(L_1,\lambda_1,L_2,\lambda_2)\times\int_0^{\infty}[G_{\kappa_2}(r)f^a_{\kappa_1}(r)\mathcal{H}^{\lambda_2}_{L_2,-\kappa_1,\kappa_2}(k_2r) -F_{\kappa_2}(r)g^a_{\kappa_1}(r)\mathcal{H}^{\lambda_2}_{L_2,\kappa_1,-\kappa_2}(k_2r)]dr , \tag{A16a}$$

$$I^{[e,\gamma]}_e=P^{[e,\gamma]}(L_2,\lambda_2,L_1,\lambda_1)\times\int_0^{\infty}[G_{\kappa_2}(r)f^e_{\kappa_1}(r)\mathcal{H}^{\lambda_1}_{L_1,-\kappa_1,\kappa_2}(k_1r) -F_{\kappa_2}(r)g^e_{\kappa_1}(r)\mathcal{H}^{\lambda_1}_{L_1,\kappa_1,-\kappa_2}(k_1r)]dr . \tag{A16b}$$

The factor $P^{[e,\gamma]}(L_1,\lambda_1,L_2,\lambda_2)$ differs in these two expressions by exchanging (L_1,λ_1) and (L_2,λ_2); it is given by

$$P^{[e,\gamma]}(L_1,\lambda_1,L_2,\lambda_2)=\tfrac{1}{2}[1+(-1)^{(l_1+l_0+L_2+\lambda_2+1)}]\tfrac{1}{2}[1+(-1)^{(l_1+l_2+L_1+\lambda_1+1)}](2j_1+1)\times\left[\frac{(2j_0+1)(2j_2+1)(2L_1+1)(2L_2+1)}{L_1(L_1+1)L_2(L_2+1)}\right]^{1/2}\begin{bmatrix}j_1 & j_0 & L_2\\ \frac{1}{2} & -\frac{1}{2} & 0\end{bmatrix}\begin{bmatrix}j_2 & j_1 & L_1\\ \frac{1}{2} & -\frac{1}{2} & 0\end{bmatrix} . \tag{A17}$$

The subscripts on the electron angular quantum numbers are 0 for the bound electron, 1 for the electron in the propagator [described by a partial wave of the F function in Eq. (A12)], and 2 for the outgoing electron. Incoming photon angular quantum numbers are denoted by subscript 1 and outgoing photon angular quantum numbers by subscript 2.

To obtain the matrix elements $I_a^{[e,\gamma]}$ and $I_e^{[e,\gamma]}$ we solve the homogeneous differential equations (A3) for radial functions G_{κ_2} and F_{κ_2} $(E>1)$, and the inhomogeneous differential equations (A14) for $g^a_{\kappa_1}$, $f^a_{\kappa_1}$ $(\eta>1)$ and $g^e_{\kappa_1}$, $f^e_{\kappa_1}$ $(\eta<1)$. We use the potential $V(r)$ and the bound-electron radial wave functions G_{κ_0} and F_{κ_0} as numerical input to our code. They can be obtained from the relativistic self-consistent calculation already discussed. Our code can use other potentials and wave functions as input.

*Present address: Theoretical Physics, The University of Tennessee, 200 South College, Knoxville, TN 37996-1501. Fax: (615) 974-6378.
Electronic address: pmb@utkvx.utk.edu
†Fax: 38(41)434-467.
Electronic address: suric@olimp.irb.hr
‡Fax: 38(41)425-497.
Electronic address: pisk@olimp.irb.hr
§Fax: (412) 624-9163.
Electronic address: rpratt@vms.cis.pitt.edu

[1] T. Surić, P. M Bergstrom, Jr., K. Pisk, and R. H. Pratt, Phys. Rev. Lett. **67**, 189 (1991).
[2] T. Surić, Nucl. Instrum. Methods A **314**, 240 (1992).
[3] P. M. Bergstrom, Jr., T. Surić, K. Pisk, and R. H. Pratt, Jr., Nucl. Instrum. Methods B **71**, 1 (1992).
[4] P. M. Bergstrom, Jr., Nucl. Instrum. Methods B (to be published).
[5] V. Marchetti and C. Franck, Phys. Rev. Lett. **59**, 1557 (1987); Phys. Rev. A **39**, 647 (1989).
[6] J. P. Briand, A. Simionvici, P. Chevallier, and P. Indelicato, Phys. Rev. Lett. **62**, 2092 (1989); A. Simionvici, J. P. Briand, P. Indelicato, and P. Chevallier, Phys. Rev. A **41**, 3707 (1990).
[7] S. Manninen, K. Hämäläinen, and J. Graeffe, Phys. Rev. B **41**, 1224 (1990).
[8] Saharsha M. Lad, G. Basavaraju, and P. P. Kane, Phys. Rev. A **42**, 1267 (1990).
[9] W. Wolff, H. E. Wolf, L. F. S. Coelho, S. de Barros, and J. Eichler, Phys. Rev. A **40**, 4378 (1989).
[10] A. J. Rollason, F. Bell, J. R. Schneider, and W. Drube, Solid State Commun. **72**, 297 (1989); A. J. Rollason, F. Bell, and J. R. Schneider, Nucl. Instrum. Methods A **281**, 147 (1989); F. Bell, A. J. Rollason, J. R. Schneider, and W. Drube, Phys. Rev. B **41**, 4887 (1990); F. Bell, Th. Tschentscher, J. R. Schneider, and A. J. Rollason, J. Phys. B **24**, L533 (1991).
[11] I. B. Whittingham, J. Phys. A **4**, 21 (1971); Aust. J. Phys. **34**, 163 (1981).
[12] L. A. Wittwer, Lawrence Radiation Laboratory Report No. UCRL-51268, Livermore, CA, 1972 (unpublished).
[13] D. W. Kosik, J. Phys. A **24**, 2259 (1991); G. E. Sneddon and I. B. Whittingham, J. Phys. B **23**, 2227 (1990); R. Mehrem, J. T. Londergan, and M. H. Macfarlane, J. Phys. A **24**, 1435 (1991); J. Vackar, A. Simunek, and O. Sipr, Comput. Phys. Commun. **66**, 259 (1991).
[14] S. A. Blundell, W. R. Johnson, and J. Sapirstein, Phys. Rev. A **37**, 2764 (1988); A. Pasquarello, L. C. Andreani, N. Binggeli, and A. Quattropani, Europhys. Lett. **17**, 387 (1992).
[15] G. E. Brown, R. E. Peierls, and J. B. Woodward, Proc. R. Soc. (London), Ser. A **227**, 51 (1955); Lynn Kissel, R. H. Pratt, and S. C. Roy, Phys. Rev. A **22**, 1970 (1980).
[16] In this paper we choose to use the natural units $\hbar=c=m=1$.
[17] H. A. Kramers and W. Heisenberg, Z. Phys. **31**, 681 (1925); I. Waller, *ibid.* **51**, 213 (1928); **58**, 75 (1929).
[18] M. Gavrila, Phys. Rev. **163**, 147 (1967); A. Costescu, Rev. Roum. Phys. **21**, 3 (1976); M. Gavrila, Z. Phys. A **293**, 269 (1979); V. Florescu and A. Cionga, Z. Phys. A **321**, 187 (1985).
[19] M. Gavrila and A. Costescu, Phys. Rev. A **2**, 1752 (1970).
[20] V. Florescu and M. Gavrila, Phys. Rev. A **14**, 211 (1976); V. Florescu, M. Marinescu, and R. H. Pratt, *ibid.* **42**, 3844 (1990).
[21] Conversely, Raman scattering into the electronic bands of solids is similar to Compton scattering in that the scattering electron is no longer confined to a given atom and so the final electronic state is quasifree. Resonant Compton scattering is the term usually applied to this scenario. In this case, the second term is resonant at energies $\omega_1 \approx E_i$ due to the presence of these valence bands immediately below the atomic continuum.
[22] Benjamin J. Bloch and Lawrence B. Mendelsohn, Phys. Rev. A **9**, 29 (1974).
[23] W. Heisenberg, Phys. Z. **19**, 737 (1931); L. Bewilogua, *ibid.* **19**, 740 (1931).
[24] F. Schnaidt, Ann. Phys. (Leipzig) **21**, 89 (1934).
[25] F. Bloch, Phys. Rev. **46**, 674 (1934).
[26] J. Randles, Proc. Phys. Soc. London Sect. A **70**, 337 (1957).
[27] P. Eisenberger and P. M. Platzmann, Phys Rev. A **2**, 415 (1970); D. A. Owen, *ibid.* **16**, 1594 (1977); Phys. Lett. **69A**, 177 (1978).
[28] M. Schumacher, Z. Phys. **242**, 444 (1971); R. Wenskus, A. Baumann, P. Rullhusen, D. Schaupp, F. Smend, and M. Schumacher, Z. Phys. A **320**, 179 (1985).
[29] M. Schumacher, F. Smend, and I. Borchert, J. Phys. B **8**, 1428 (1975); Comput. Phys. Commun. **11**, 363 (1976).
[30] Roland Ribberfors, Phys. Rev. B **12**, 2067 (1975); *ibid.* **12**, 3136 (1975).
[31] M. Pradoux, H. Meunier, M. Avan, and G. Roche, Phys. Rev. A **16**, 2022 (1977).
[32] M. Gavrila, Lett. Nuovo Cimento **5**, 180 (1969); Phys. Rev. A **6**, 1348 (1972); **6**, 1360 (1972); Rev. Roum. Phys. **19**, 473 (1974).
[33] A. Costescu and M. Gavrila, Rev. Roum. Phys. **18**, 493 (1973); M. Gavrila and M. N. Tugulea, *ibid.* **20**, 209 (1975).
[34] A. Costescu, F. D. Aaron, I. Schneider, and I. N. Mihalescu, Opt. Lett. **11**, 449 (1986).
[35] F. E. Low, Phys. Rev. **110**, 974 (1958).
[36] J. M. Jauch and F. Rohrlich, *The Theory of Photons and Electrons: The Relativistic Quantum Field Theory of*

Charged Particles with Spin One-Half, 2nd ed. (Springer-Verlag, New York, 1976); T. H. Burnet and N. M. Kroll, Phys. Rev. Lett. **20**, 86 (1968).

[37] For a discussion and review of non-IPA treatments of this region, see T. Aberg and J. Tulkki, in *Atomic Inner Shell Physics,* edited by B. Crasemann (Plenum, New York, 1985).

[38] Recent reviews of Compton scattering measurements have been given by M. Chakrabarty, R. H. Pratt, S. C. Roy, and S. K. Sen Gupta, Trans. Bose Inst. **54**, 1 (1991); P. P. Kane, Phys. Rep. **218**, 67 (1992).

[39] W. Mehlhorn, in *X-Ray and Atomic Inner-Shell Physics-1982,* Proceedings of the International Conference on X-Ray and Atomic Inner-Shell Physics, 1982, edited by B. Crasemann, AIP Conf. Proc. No. 94 (AIP, New York, 1982), p. 53.

[40] A. Ljubičić, K. Ilakovac, V. Knapp, and K. Pisk, in *Symposium on Nuclear Beta Decay and Weak Interactions, Zagreb, 1967,* edited by B. Eman and D. Tadic (Institute "Ruđer Bošković," Zagreb, 1967), p. 285.

[41] G. Cross and N. F. Ramsey, Phys. Rev. **80**, 929 (1950).

[42] Arthur H. Compton, Phys. Rev. **21**, 483 (1923); **22**, 409 (1923).

[43] O. Klein and Y. Nishina, Z. Phys. **52**, 853 (1929).

[44] J. W. M. DuMond, Phys. Rev. **33**, 643 (1929).

[45] F. Biggs, L. B. Mendelsohn, and J. B. Mann, At. Data Nucl. Data Tables **16**, 201 (1975).

[46] P. Eisenberger and W. A. Reed, Phys. Rev. B **9**, 3237 (1974).

[47] S. Manninen, T. Paakkari, and K. Kajante, Philos. Mag. **29**, 167 (1974).

[48] J. H. Hubbell, Wm. J. Veigele, E. A. Briggs, R. T. Brown, D. T. Cromer, and R. J. Howerton, J. Phys. Chem. Ref. Data **4**, 471 (1975).

[49] R. Ribberfors and K.-F. Berggren, Phys. Rev. A **26**, 3325 (1982).

[50] R. H. Pratt and C. M. Lee, Phys. Rev. A **16**, 1733 (1977).

[51] Leonard Rosenberg, Phys. Rev. A **44**, 2949 (1991).

[52] Leonard Rosenberg and Fei Zhou, Phys. Rev. A **44**, 7283 (1991).

[53] James McEnnan and Mihai Gavrila, Phys. Rev. A **15**, 1537 (1977).

[54] Guy C. Spitale and Stewart D. Bloom, Phys. Rev. A **16**, 221 (1977).

[55] G. Basavaraju, P. P. Kane, and Suju M. George, Phys. Rev. A **36**, 655 (1987).

[56] A. F. Kodre and S. M. Shafroth, Phys. Rev. A **19**, 675 (1979).

[57] D. Liberman, D. Cromer, and J. Waber, Comput. Phys. Commun. **2**, 107 (1971).

[58] H. K. Tseng and R. H. Pratt, Phys. Rev. A **3**, 100 (1971).

[59] P. Holm and R. Ribberfors, Phys. Rev. A **40**, 6251 (1989).

[60] E. Fermi, Rev. Mod. Phys. **4**, 87 (1932).

[61] A. Bechler and R. H. Pratt, Phys. Rev. A **39**, 1774 (1989).

[62] E. Henry, Ph.D. thesis, University of Colorado, 1969.

[63] J. H. Scofield, Lawrence Radiation Laboratory Report No. UCRL-51326, Livermore, CA, 1973 (unpublished).

[64] D. J. Botto and M. Gavrila, Phys. Rev. A **26**, 237 (1982).

[65] D. E. Cullen, M. H. Chen, J. H. Hubbell, S. T. Perkins, E. F. Plechaty, J. A. Rathkopf, and J. H. Scofield, Lawrence Livermore National Laboratory Report No. UCRL-50400, Vol. 6, Rev. 4, Livermore, CA, 1989 (unpublished).

[66] S. T. P. V. J. Swamy and D. S. R. Murty, Phys. Lett. **55A**, 17 (1975); Physica **84B**, 289 (1976); G. Basavaraju, S. M. George, and P. P. Kane, Nucl. Instrum. Methods **193**, 631 (1982).

[67] Vincent Marchetti and Carl Franck, Phys. Rev. Lett. **65**, 268 (1990); J. P. Briand, A. Simionovici, P. Chevallier, and P. Indelicato, *ibid.* **65**, 269 (1990).

[68] James D. Bjorken and Sidney D. Drell, *Relativistic Quantum Mechanics* (McGraw-Hill, New York, 1964).

[69] Albert Messiah, *Quantum Mechanics* (Wiley, New York, 1968).

[70] A. I. Akhiezer and V. B. Berestetskii, *Quantum Electrodynamics* (Interscience, New York, 1965).